

# Black hole binaries in galactic nuclei and gravitational wave sources

Jongsuk Hong<sup>1,2\*</sup>, Hyung Mok Lee<sup>1,3\*</sup>

<sup>1</sup>*Astronomy Program, Department of Physics and Astronomy, Seoul National University, 1 Gwanak-ro, Gwanak-gu, Seoul 151-742, Korea*

<sup>2</sup>*Department of Astronomy, Indiana University, Bloomington, IN 47404-7105, USA*

<sup>3</sup>*Center for Theoretical Physics, Seoul National University, 1 Gwanak-ro, Gwanak-gu, Seoul 151-742, Korea*

Accepted 2015 January 6. Received 2014 December 9; in original form 2014 July 31

## ABSTRACT

Stellar black hole (BH) binaries are one of the most promising gravitational wave (GW) sources for GW detection by the ground-based detectors. Nuclear star clusters (NCs) located at the centre of galaxies are known to harbour massive black holes (MBHs) and to be bounded by a gravitational potential by other galactic components such as the galactic bulge. Such an environment of NCs provides a favourable conditions for the BH-BH binary formation by the gravitational radiation capture due to the high BH number density and velocity dispersion. We carried out detailed numerical study of the formation of BH binaries in the NCs using a series of N-body simulations for equal-mass cases. There is no mass segregation introduced. We have derived scaling relations of the binary formation rate with the velocity dispersion of the stellar system beyond the radius of influence and made estimates of the rate of formation of black hole binaries per unit comoving volume and thus expected detection rate by integrating the binary formation rate over galaxy population within the detection distance of the advanced detectors. We find that the overall formation rates for BH-BH binaries per NC is  $\sim 10^{-10} \text{ yr}^{-1}$  for the Milky-Way-like galaxies and weakly dependent on the mass of MBH as  $\Gamma \propto M_{\text{MBH}}^{3/28}$ . We estimate the detection rate of  $0.02\text{--}14 \text{ yr}^{-1}$  for advanced LIGO/Virgo considering several factors such as the dynamical evolution of NCs, the variance of the number density of stars and the mass range of MBH giving uncertainties.

**Key words:** gravitational waves — methods: numerical — galaxies: nuclei.

## 1 INTRODUCTION

The gravitational wave (GW) is the propagation of ripples of the space-time curvature with speed of light. Although Einstein (1916) predicted the existence of gravitational radiation (GR), the GWs have never been directly detected yet. From 30 years observations, Weisberg & Taylor (2005) found that the binary pulsar PSR 1913+16, discovered by Hulse & Taylor (1974), exhibited the decrease of the orbital period and the amount of decrease exactly coincide with the prediction of general relativity. There are several types of astronomical objects that can produce significant amount of gravitational waves: core-collapse supernovae (e.g., Mueller & Janka 1997; Yakunin et al. 2010), spinning neutron stars (e.g., Andersson et al. 2011), compact binary coalescences (e.g., Kalogera et al. 2004), supermassive black holes (SMBH) (e.g., binary SMBH merger, Berentzen et al. 2009) (extreme mass ratio inspirals, EMRI, Hopman & Alexander 2006; Merritt et al. 2011) and cosmological density fluctuations (e.g., Ananda et al. 2007). Among those, the compact binary coalescence (CBC) involving neutron stars (NS) or stellar mass BH is the primary targets for the second generation of ground based detectors such as advanced LIGO and Virgo. Up to now, only ten NS-NS binary pulsars have

been discovered in our Galaxy including PSR 1913+16, and a half of them will merge within a Hubble time (O’Shaughnessy et al. 2010). Based on these binaries and theoretical studies, the rate of NS-NS merger within the horizon of the advanced detectors is estimated to lie between 0.4 and 100 per year (Abadie et al. 2010). These NS-NS binaries are thought to have been evolved from primordial binaries. Obviously other types such as BH-NS and BH-BH binaries can form by the evolution of binaries of high mass stars, but their rates are highly uncertain especially because of the lack of observed systems. Since the detection of the GWs coming from the CBC event will provide us with the information regarding the masses of the binaries, we should be able to distinguish different types of binaries through the observations of GWs in the future.

Compact binaries can also be formed dynamically in stellar systems: three-body processes and dissipative two-body processes by tidal effect (Lee & Ostriker 1986) or GW emission (hereafter GR capture, Hansen 1972; Quinlan & Shapiro 1987). Stellar systems such as globular clusters (GC) and nuclear star clusters (NC) at the galactic nuclei provide good environments for the dynamical formation of compact binaries. In GCs, when the core is dense enough, compact binaries can be formed by three-body encounters. These binaries become more compact through close encounters with other stars and is eventually kicked out from GCs when their orbital separations become very small. Some of the ejected bi-

\* E-mail: jshong@astro.snu.ac.kr (JH); hmllee@snu.ac.kr (HML)

naries merge within a Hubble time in galactic field (Banerjee et al. 2010; Downing et al. 2011; Bae et al. 2014). On the other hand, binary formation by three-body processes is suppressed by the existence of massive BH (MBH) in galactic nuclei (Baumgardt et al. 2004a). Instead, coalescences of primordial compact binaries can be driven by the orbit coupling with central MBH, as known as the Kozai effect (Kozai 1962), and could occur within Hubble time (Antonini & Perets 2012). Compact binaries, especially BH-BH binaries, also can be formed by GR capture in NCs due to the high stellar density and velocity dispersion at the vicinity of MBH (O’Leary et al. 2009). The black holes are expected to be highly concentrated in the central parts through the dynamical friction against low mass stars, providing a favorable environment for the close encounters between black holes. Such captured compact binaries usually have large eccentricities with small pericentre distance, and thus, their waveforms will be different from the ones produced by the circular binaries (Abramovici et al. 1992).

Numerous authors made estimates of the detection rates of GWs from CBCs with present- and planned- GW detectors using various methods: population synthesis models for primordial binaries (Kalogera et al. 2004; Belczynski et al. 2007), Monte-Carlo simulations for GCs (Downing et al. 2011) and Fokker-Planck simulations for NCs (O’Leary et al. 2009), and estimated that a few tens of events will be detected by new generation GW detectors every year (see, for example, Abadie et al. 2010). However, most of these studies are based on simplified models and assumptions on the evolution of the stellar systems and the binaries. There remain substantial uncertainties because of difficulties in accurately modeling of the systems with the large number of stars. Direct  $N$ -body approach is impossible for realistic systems, and therefore, statistical approaches such as Fokker-Planck models and Monte-Carlo simulations have been used, so far. In this paper, we focus on the binary formation of BHs by GR capture in NCs by direct  $N$ -body simulations. Although, we cannot use realistic number of stars, we try to deduce important information regarding the binary formation and evolution based on scaled-down and simplified version of  $N$ -body simulations. Our study should provide useful comparison with the statistical models.

This paper is organized as follows. In §§2 and 3, we introduce the numerical method and the model for star clusters in galactic nuclei with a central MBH. The dynamical evolution of our model is presented in §4. In §5, we describe binary formation in NCs and estimate the merger rate per galaxy. In §6, the expected detection rate for new generation GW detectors is estimated. To give the interpretation for binary coalescences and their waveforms, we implement post-Newtonian approximations on the two-body motions. An example waveform of a binary BH coalescence in Milky-Way-like galaxies is provided in §7. Finally, we summarize in §8.

## 2 INITIAL MODELS

NCs are very dense stellar systems located at the nuclei of galaxies, regardless of the type (e.g., Carollo et al. 1997; Böker et al. 2002; Côté et al. 2006). Their typical mass is  $10^{6-7} M_{\odot}$  (Walcher et al. 2005), the size of NCs is comparable to that of galactic GCs (Böker et al. 2004; Côté et al. 2006), thus average stellar density of NCs is much higher than GCs. It is also well known that most of galaxies host MBHs at the centre (e.g., Kormendy & Richstone 1995; Ferrarese & Ford 2005). The coexistence and correlation of MBHs and NCs at the central region of galaxies have been studied by Graham & Spitler (2009).

Observational (e.g., Schödel et al. 2009) and theoretical (e.g., Bahcall & Wolf 1976) studies for star clusters with the central MBH showed that the density and velocity dispersion increases steeply toward the MBH, following Kepler’s profile (i.e.,  $\sigma \propto r^{-1/2}$ ). The modeling of stellar systems with a central black hole has been done by numerous authors (e.g., Young 1980; Goodman & Binney 1984; Quinlan et al. 1995; Sigurdsson et al. 1995; Holley-Bockelmann et al. 2002). In order to generate  $N$ -body realizations for NCs with MBH, we adopt ‘adiabatic growth’ of the MBH as suggested by Sigurdsson et al. (1995). The MBH is assumed to grow with time as

$$M_{\text{MBH}}(t) = \begin{cases} M_{\text{MBH}} \left[ 3 \left( \frac{t}{t_{\text{MBH}}} \right)^2 - 2 \left( \frac{t}{t_{\text{MBH}}} \right)^3 \right] & t \leq t_{\text{MBH}} \\ M_{\text{MBH}} & t > t_{\text{MBH}} \end{cases} \quad (1)$$

where  $M_{\text{MBH}}$  and  $t_{\text{MBH}}$  are the final mass of MBH and the black hole growth time scale, respectively. During the growth of the MBH, the stellar system is adjusted against the potential of the MBH. The MBH is fully grown after  $t_{\text{MBH}}$ , and the gravitational potential of the MBH is assumed to follow that of the Plummer model

$$\phi_{\text{MBH}} = - \frac{GM_{\text{MBH}}}{\sqrt{r^2 + \varepsilon_{\text{MBH}}^2}} \quad (2)$$

where  $\varepsilon_{\text{MBH}}$  is the softening parameter for avoiding unexpected effect at the singularity. Sigurdsson et al. (1995) noted that  $t_{\text{MBH}}$  should be larger than the half-mass dynamical time to ensure the adiabatic growth of the MBH. While they used the Hernquist model as the initial density distribution, we used Plummer model with half-mass dynamical time  $t_{\text{dyn},1/2} \sim 2.46$  for standard  $N$ -body scaling (i.e.,  $G = M_{\text{cl}} = -4E = 1$ ).

According to recent observations (e.g., Schödel et al. 2009) of the centre of the Milky Way (i.e., the vicinity of Sgr A\*), the velocity dispersion of stars at about 1 parsec scale is nearly flat. This implies that the NC is almost in the isothermal state. However, it is not possible for the isolated stellar systems to become fully isothermal. In order to realize nearly isothermal sphere we need a very large and massive system. Instead we model the NC as a isothermal sphere surrounded by external potential which is assumed to be fixed. Such an external potential could be provided by the galactic bulge. Yoon et al. (2011) have investigated a self-gravitating stellar systems embedded in an external potential well. They considered a Plummer external potential,

$$\phi_{\text{pl}} = - \frac{GM_{\text{pl}}}{\sqrt{a_{\text{pl}}^2 + r^2}} \quad (3)$$

where  $M_{\text{pl}}$  and  $a_{\text{pl}}$  are the mass and scale length of the Plummer potential, respectively. They revealed that if the external potential well is deep enough compared to the potential of embedded stellar system, the external potential well behaves like a heat bath. The velocity dispersion of the embedded stellar system, therefore, becomes isothermal and there exists a quasi-equilibrium solution of a potential-density pair for the nearly isothermal stellar system (see Model 2 of Fig. 10 in Yoon et al. 2011).

The bulge is one of galactic components, extending over few kpc scales. NC and bulge are independent components of galaxies with different surface brightness profiles (e.g., Balcells et al. 2003). In the Milky way, the effective radius (i.e., half-light radius) of the bulge is about 0.1 kpc, and the mass is estimated to be roughly  $10^{10} M_{\odot}$ . According to a dynamical model of Galactic bulge suggested by Kent (1992), the kinematics of the bulge is affected by

the MBH, Sgr A\*, at inner parsec scale, and the velocity dispersion is nearly flat from 1 to 10 parsec and increases gradually at the large radii. We assume that the the bulge is a sphere in this study for the simplicity. This may not cause a serious effects on the dynamics of the nuclear cluster we are considering since the role of the bulge in our model is to confine the nuclear cluster within a few parsec.

### 3 COMPUTATIONAL METHODS

In this study, we used the GPU accelerated version of NBODY6 (Nitadori & Aarseth 2012). This code includes many efficient and accurate algorithms such as the fourth-order Hermite integrator, the individual and block time steps, the Ahmad-Cohen neighbor scheme, the Kustaaheimo-Stiefel (KS) and chain regularization scheme (Aarseth 1999). Recently, by using numerous stream processors of GPU devices, calculations of gravitational interactions among stars have been significantly accelerated through massive parallelism. Force calculation in NBODY6 code is divided into *regular* force from distant particles whose gravitational potential change slowly and *irregular* force from neighboring particles that give strong gravitational fluctuations. In the GPU accelerated version, the regular forces are calculated by GPU machines with single precision while irregular force calculation that needs better accuracy is still done by CPUs.

As we mentioned above, the external potential is composed of two parts,

$$\phi_{\text{ext}} = \phi_{\text{MBH}} + \phi_{\text{Pl}} \quad (4)$$

where  $\phi_{\text{MBH}}$  is the Keplerian potential due to the central MBH. In our implementation, these external forces are added to the sum of regular forces.

All the calculations in NBODY6 code use dimensionless time, length and mass units. From given unit of length  $\bar{r}$  in parsec and mean stellar mass  $\bar{M}$  in  $M_{\odot}$ , the physical unit of velocity and time can be expressed as (Aarseth 2010)

$$\text{velocity} : 6.557 \times 10^{-2} \left( \frac{N\bar{M}}{\bar{r}} \right)^{1/2} \text{ km/s,}$$

$$\text{time} : 14.94 \left( \frac{\bar{r}^3}{N\bar{M}} \right)^{1/2} \text{ Myr} \quad (5)$$

where  $N$  is total number of stars.

Table 1 shows model parameters of our simulations. Although galactic nuclei contain  $\sim 10^6$  stars in a cubic parsec, it is hard to treat such a large number of particles for NBODY6 code even with GPU machine. We, therefore, used several different number of particles ranging from 10,000 to 100,000 in order to build a scaling relation. We also made several simulations with different random seeds and took average in order to reduce the statistical noises. The masses of MBH are chosen to be 10 and 20 % of the entire mass of cluster stars  $M_{\text{cl}}$  (but excluding the mass of the Plummer potential). Because these masses are relatively larger than those of Sigurdsson et al. (1995) and Holley-Bockelmann et al. (2002), we also used longer black hole growth time scale  $t_{\text{MBH}} = 50$ . The softening parameter of the MBH is fixed to  $10^{-4}$ , which is much smaller than the radius of influence of the MBH (c.f.,  $r_{\text{inf}} \equiv M_{\text{MBH}}/\sigma_*^2 \sim 0.1$  for  $M_{\text{MBH}} = 0.1$ ). We assumed that all stars have same masses (i.e.,  $m = 1/N$ ) of stellar mass BHs with the mass of  $10M_{\odot}$ . Thus, the total mass of the cluster in physical unit

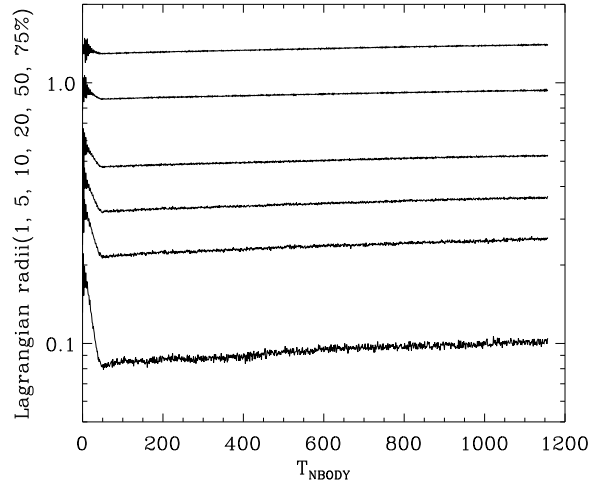


**Figure 1.** Time evolution of Lagrangian radii for the star cluster with a growing central MBH and an external Plummer potential well. By the growth of MBH, the Lagrangian radii decrease with time until  $T = t_{\text{MBH}} = 50$ . After full growth of the MBH, the cluster expands due to the heating from the MBH and stars in the cusp.

becomes  $M_{\text{tot}} = 10NM_{\odot}$ . It is well known that there is a correlation between the mass of MBHs and the kinematics of bulges. Recently, McConnell & Ma (2013) updated the  $M_{\text{MBH}} - M_{\text{bulge}}$  relation and found that the mass of MBH is roughly 0.2% of the bulge mass for  $10^7 < M_{\text{MBH}}/M_{\odot} < 10^{10}$  (also see Graham & Scott 2015). For the external potential of a bulge, we fixed the mass and scale length of the Plummer potential to 100 and 5, respectively, which corresponds to  $M_{\text{MBH}}/M_{\text{bulge}} = 0.001$  and  $0.002$  for our models. Under this potential well, the embedded stellar system is expected to become nearly isothermal in a few half-mass relaxation time (Yoon et al. 2011). We also considered a model without the external Plummer potential well (Model 0) for the purpose of comparison.

## 4 DYNAMICAL EVOLUTION OF STAR CLUSTERS

### 4.1 Cluster expansion

In order to investigate the effect of the MBH and the surrounding bulge, the dynamical evolution of the star cluster is presented in this section. Here, we focus on the Model 4 with  $N = 100,000$  and  $M_{\text{MBH}}/M_{\text{cl}} = 0.2$ .

Fig. 1 shows the time evolution of Lagrangian radii including 1, 5, 10, 20, 50 and 75 % of total cluster mass. Before  $T = t_{\text{MBH}} = 50$ , all Lagrangian radii decrease with growth of the central MBH to adjust with the strong potential of the MBH. After  $T = t_{\text{MBH}}$ , Lagrangian radii increase gradually as reported in previous studies (e.g., Baumgardt et al. 2004a; Freitag et al. 2006; Fiestas et al. 2012). The basic mechanism of the expansion is similar to that of post core collapse expansion of star clusters. With the MBH, kinetic energy can be generated by stars in the cusp (Shapiro 1977). The MBH and the innermost star can behave like hard binaries in the core of star clusters. Encountering other single stars in the cusp, they are to be bounded stronger and convert their internal energy to the kinetic energies of stars in the cusp. The kinetic energies are transferred to the whole cluster via relaxation.

While the kinetic, potential and total energies of an isolated

**Table 1.** Initial parameters for all models.

| Model | $N_{\text{cl}}$<br>(1) | $N_{\text{run}}$<br>(2) | $M_{\text{MBH}}/M_{\text{cl}}$<br>(3) | $M_{\text{MBH}}/m_*$<br>(4) | $t_{\text{MBH}}$<br>(5) | $\varepsilon_{\text{MBH}}$<br>(6) | $M_{\text{pl}}$<br>(7) | $a_{\text{pl}}$<br>(8) |
|-------|------------------------|-------------------------|---------------------------------------|-----------------------------|-------------------------|-----------------------------------|------------------------|------------------------|
| 0     | 100,000                | 1                       | 0.2                                   | 10,000                      | 50                      | $10^{-4}$                         | -                      | -                      |
| 1     | 10,000                 | 10                      | 0.2                                   | 2,000                       |                         |                                   |                        |                        |
| 2     | 20,000                 | 5                       | 0.2                                   | 4,000                       |                         |                                   |                        |                        |
| 3     | 50,000                 | 2                       | 0.2                                   | 10,000                      |                         |                                   |                        |                        |
| 4     | 100,000                | 1                       | 0.2                                   | 20,000                      | 50                      | $10^{-4}$                         | 100                    | 5                      |
| 5     | 20,000                 | 5                       | 0.1                                   | 2,000                       |                         |                                   |                        |                        |
| 6     | 50,000                 | 2                       | 0.1                                   | 5,000                       |                         |                                   |                        |                        |
| 7     | 100,000                | 1                       | 0.1                                   | 10,000                      |                         |                                   |                        |                        |

Notes. (1): Number of stars in the nuclear star cluster. (2): Number of simulations with different initial random seeds. (3): MBH mass compared to the total mass of cluster. (4) Mass ratio of MBH to the stellar mass. (5): MBH growth time scale. (6): Softening parameter of MBH potential. (7): Mass of external Plummer potential. (8): Scale length of external Plummer potential.

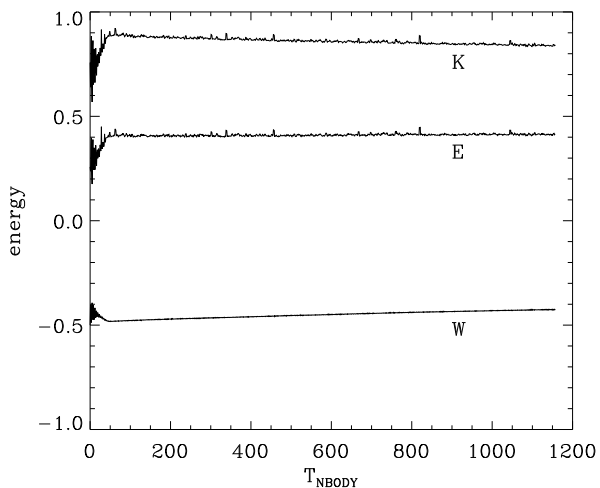


**Figure 2.** Time evolution of energies for stellar particle only. To be virialized against the external potential, the kinetic energy becomes much larger than the isolated systems. The kinetic energy decreases with time because of the cluster expansion while the total energy is nearly conserved.

self gravitating system are 1/4, -1/2 and -1/4 in NBDY units, respectively, the system embedded in a potential well has larger kinetic energy than the isolated system through the virialization (Yoon et al. 2011). Also, when the kinetic energy is even larger than the magnitude of the potential energy (i.e., the total energy becomes positive), the system will not reach the core collapse. Fig. 2 shows the time evolution of the energies. Our models are designed to have positive total energy. Initially, the kinetic energy, potential energy of self-gravity and total energy are 0.7, -0.45 and 0.25, respectively. However, as the black hole grows, the potential energy decreases because the cluster becomes more centrally concentrated as shown in Fig. 1 while the kinetic energy increases in response to the external potential of the bulge. At  $T = t_{\text{MBH}}$ , the energies become -0.5 (potential), 0.9 (kinetic) and 0.4 (total), respectively. The potential energy increases after  $T = t_{\text{MBH}}$  due to the cluster expansion although we designed a quasi-equilibrium model by using the external Plummer potential. Once the MBH has

been grown, the numerical error is generated by the interaction between the innermost stars and the MBH at  $r \rightarrow 0$ . For Model 4, the root-mean-square (RMS) error of total energy per step  $\langle \Delta E/E \rangle_{\text{rms}}$  including the potential energies from external potential and MBH is  $\sim 10^{-3}$ , overall. Such a large error could originate in escaping stars which are kicked out from inner region due to the less accurate force calculation during the regularization processes perturbed by strong gravitational potential of the MBH. However, they have very large escaping velocity ( $\sim 100\sigma_*$ ) and rarely interact with other stars during escaping. When these escapers are excluded, the RMS error drops to  $\sim 10^{-6}$ . Although these escapers rarely interact with other stars, the indirect heating could cause small structural changes at  $r < 10^{-2}$  where escapes mostly happen, as discussed in §5.2.

## 4.2 Radial profiles

In order to describe the dynamics at the vicinity of MBH, it is very important to determine the radius of influence  $r_{\text{inf}}$ , within which stars are directly affected by the gravitational potential of MBH. We estimated the radius of influence by following the definition of Baumgardt et al. (2004a) as

$$r_{\text{inf}} = \frac{GM_{\text{MBH}}}{2\sigma_*^2} \quad (6)$$

where ‘2’ is an empirical factor suggested by Baumgardt et al. (2004a), and  $\sigma_*$  is here the density-weighted one dimensional velocity dispersion of stars

$$\sigma_*^2 \equiv \frac{\int_{r_{\text{inf}}}^{r_{\text{half}}} 4\pi\sigma^2(r)\rho(r)r^2 dr}{\int_{r_{\text{inf}}}^{r_{\text{half}}} 4\pi\rho(r)r^2 dr} \quad (7)$$

where  $r_{\text{half}}$  is half-mass radius. Since  $r_{\text{inf}}$  and  $\sigma_*$  are interrelated each other, the estimation of them is made iteratively within the relative error  $10^{-4}$ . For instance,  $r_{\text{inf}} = 0.16$ ,  $\sigma_* = 0.79$  and the mass of stars within  $r_{\text{inf}}$ ,  $M(< r_{\text{inf}}) \approx 0.3$  for Model 4, respectively.

In Fig. 3, we show the density profile of the star cluster of the Model 4 for  $t = 0$  and  $1000T_{\text{NBDY}}$ . We see in Figs. 1 and 2 that the cluster is not in equilibrium but expanding. However, as reported in Baumgardt et al. (2004a), the equilibrium profile is expected to be established from inner to outer regions after a few local relaxation times (c.f.,  $\tau_{\text{ri}} \sim 100$  and  $\tau_{\text{rh},0} \sim 1600T_{\text{NBDY}}$  for

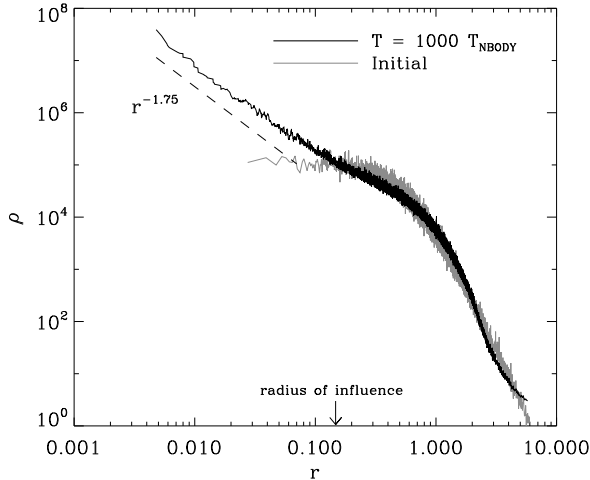


**Figure 3.** Density profiles at  $T = 0$  and  $T = 1000T_{\text{NBODY}}$ . Grey line shows the initial condition. Because of the existence of MBH, the stellar cusp, so-called Bahcall-Wolf cusp, is formed inside the radius of influence. Our model has less steep density profile when approaching  $r_{\text{inf}}$  than the theoretical profile of  $r^{-1.75}$  due to the contamination from outer parts.

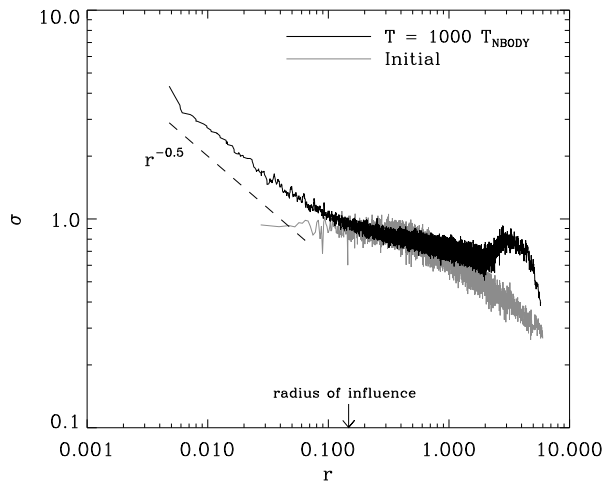


**Figure 4.** Velocity dispersion profiles at two epochs:  $T = 0$  and 1000. The existence of MBH makes stars within radius of influence follow the Keplerian profile. For the outer parts, the velocity dispersion is flatter than the initial condition due to the external potential well.

Model 4). The radius of influence  $r_{\text{inf}}$  is marked as the downward arrow. The slope of density cusp at  $r \ll r_{\text{inf}}$  is similar to -1.75 for equal-mass systems but becomes shallower at  $r \rightarrow r_{\text{inf}}$ . This feature has already been observed many previous studies with different approaches such as direct  $N$ -body (Baumgardt et al. 2004a) and Monte-Carlo simulations (Freitag et al. 2006). There is an up-turn of the density near  $r = 5$ . This radius is the scale length of the external Plummer potential, so stars have piled up at this radius against the external force from the potential.

The radial profile of velocity dispersion is presented in Fig. 4. The black line shows the profile at  $T = 1000$ , and the grey line is the initial one. For the outer part in Fig. 4, the velocity dispersion is not completely flat, but flatter than the initial profile. There is a

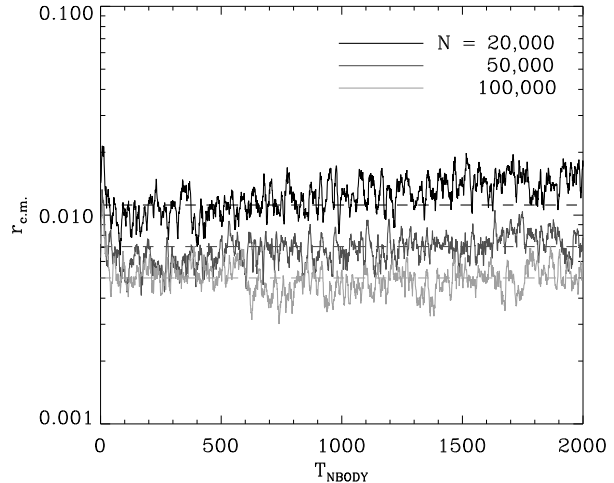


**Figure 5.** Separation between the MBH and the centre of mass of stars as a function of time for simulations with different  $N$ . Contrasts show different numbers of stars. With less number of stars, the MBH wanders more. Dashed lines represent the wandering radius based on the our scaling relation obtained from  $N=100,000$  model.

bump of velocity dispersion at  $r \sim 5$ , the scale length of the external Plummer potential. This may have been caused by the heating effect by the external potential which is more effective where the depth of the external potential acts like a reflecting wall. This will be more evident in the next subsection on the velocity anisotropy. The heating through the reflection would appear mostly in the radial direction. When the MBH exists, stars inside  $r_{\text{inf}}$  are strongly affected by the MBH, and their velocity dispersion follows the Keplerian profile (i.e.,  $\sigma(r) \sim r^{-0.5}$ ). However, the slope is a little shallower than the expectation as similar to the density profile in Fig. 3. Another important characteristic of MBH surrounded by stars is the wandering. An MBH in a stellar system can move randomly, like a Brownian motion, by the interaction with stars which are bounded and un-bounded to the potential of the MBH. In addition, the MBH and the innermost star can play a role as binaries in the core-collapsed star cluster. They kick a star interacting with them with high kinetic energy, and this causes the recoil motion of the MBH. Lin & Tremaine (1980) investigated the motion of the MBH in the stellar system such as a globular cluster and concluded that the interaction with unbound stars is the most important effect causing the motion of the MBH. Bahcall & Wolf (1976) estimated the uncertainty of the position of the MBH by the wandering of the MBH as

$$r_{\text{wand}} \approx 0.92 r_c \sqrt{m_*/M_{\text{MBH}}} \quad (8)$$

where  $r_c$  is the core radius. It is difficult to define the wandering radius in our simulations because there is not a well-defined core, but Fiestas et al. (2012) found the empirical relation for the MBH wandering radius as  $r_{\text{wand}} = 0.5(m_*/M_{\text{MBH}})^{0.5}$  for King models.

Fig 5 shows the wandering radius estimated by the radial distance of the MBH fixed at the origin to the centre of mass of the stellar particles. The solid lines are the wandering radius in the simulations for the simulations with different number of stars ranging from 20,000 (top) to 100,000 (bottom) with the MBH mass of 0.2. As the number of stars becomes larger, the wandering radius becomes smaller as shown in equation (8). The dashed lines are

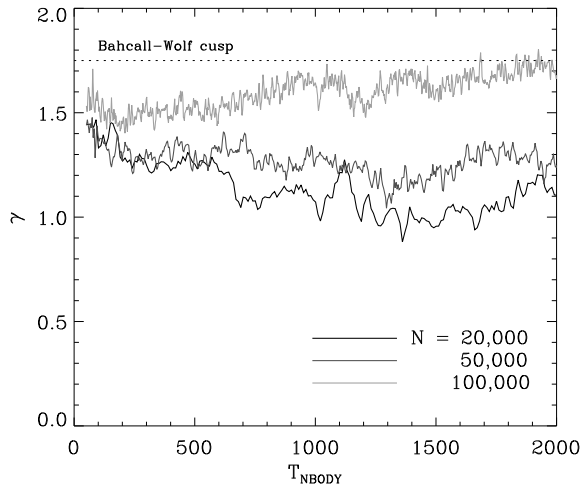


**Figure 6.** Time evolution of the slope of stellar cusp within the radius of influence (see text). Different lines show results with different numbers of stars. There is a tendency of steeper slope for the larger  $N$  models. The model with  $N=100,000$  reaches the Bahcall-Wolf slope at  $T \sim 2000$ .

the values obtained with the relation from Fiestas et al. (2012), but with different coefficient of 0.7 rather than 0.5. Thus the wandering radius follows the scaling relation with  $N$  very well. Different coefficient is likely to be from the different initial profiles. The time evolution of the slope of the central stellar cusp  $\gamma$  is shown in Fig. 6. Due to the fact that the density cusp is smeared out by the random walk of MBH (Fiestas et al. 2012) and the density profile is contaminated by outer region at  $r \rightarrow r_{\text{inf}}$  as shown in Fig. 3, the slope is estimated with the stars at  $r_{\text{wand}} < r < 0.3r_{\text{inf}}$  (However, we used larger factor rather than 0.3 for small  $N$  runs to secure enough number of stars in that range, and this may cause shallower cusp for small  $N$  runs). Different contrasts mean different number of stars. For larger  $N$ , the slope increases with time slowly toward the Bahcall-Wolf value of -1.75 while those with smaller  $N$  do not get close to the Bahcall-Wolf cusp. For Model 4, the cusp once approaches to the Bahcall-Wolf cusp at  $T = 2000T_{\text{NBODY}}$ . This is consistent with the result of Freitag et al. (2006) that it takes order  $10\tau_{\text{Ti}}$  (c.f.,  $\tau_{\text{Ti}} \sim 100$ ) for the Bahcall-Wolf cusp to be fully-developed. However, it is still true that most of our models have shallower cusps overall. The shallower stellar cusp will affect the merger rate of stellar mass BHs near the MBH as discussed in the next sections.

### 4.3 Velocity anisotropy

It is well known that the radial anisotropy in the velocity dispersion increases at the outer part of isolated stellar systems as a result of two-body relaxation (Giersz & Heggie 1996; Spitzer 1987). The anisotropy parameter can be defined by (Binney & Tremaine 2008)

$$\beta \equiv 1 - \frac{\sigma_t^2}{2\sigma_r^2} \quad (9)$$

where  $\sigma_t$  and  $\sigma_r$  are the tangential and radial velocity dispersion, respectively. This anisotropy parameter varies from  $-\infty$  (purely circular orbits) to  $+1$  (purely radial orbits). Also, in a tidal field, the radial anisotropy decreases during post core-collapse expansion due to the loss of radial orbits (Takahashi et al. 1997). However, in the case of stellar systems with a growing central massive object,

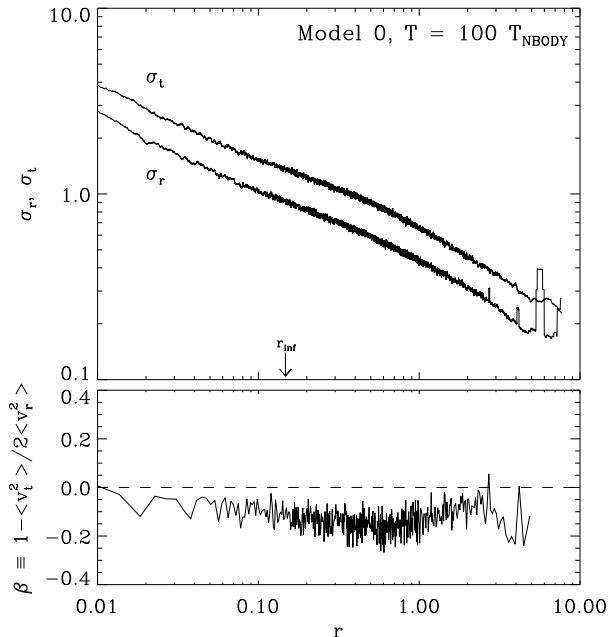


**Figure 7.** Profiles of Radial and tangential velocity dispersion (upper) and the anisotropy parameter (lower) for Model 0 without the external Plummer potential. The velocity distribution is tangentially biased, and the profile is similar to that of the isochrone model in Quinlan et al. (1995) except for the position of maximum anisotropy.

the tangential anisotropy is developed (i.e.,  $\beta < 0$ , Young 1980; Goodman & Binney 1984; Quinlan et al. 1995; Sigurdsson et al. 1995; Holley-Bockelmann et al. 2002). Quinlan et al. (1995) have revealed that the aspect of anisotropy is affected by the initial models. For models with a core such as isothermal sphere and isochrone model, the velocity distribution becomes isotropic in the limit  $r \rightarrow 0$  (Young 1980; Quinlan et al. 1995). On the other hand, for ‘two-power’ models for galaxies like Dehnen’s models (Dehnen 1993), the velocity distribution is still tangentially biased at  $r \rightarrow 0$  (Quinlan et al. 1995; Sigurdsson et al. 1995; Holley-Bockelmann et al. 2002). The tangential anisotropy reaches the peak at  $r \approx r_{\text{inf}}$ , and the velocity distribution becomes isotropic at  $r \gg r_{\text{inf}}$  again (see Figs. 2-5 of Quinlan et al. 1995).

The radial and tangential velocity dispersion and the velocity anisotropy parameter after the growth of MBH are shown in Fig. 7 for the Model 0 without the external Plummer potential and Fig 8 for the Model 4 with the potential, respectively. For the Model 0, the velocity dispersion decrease rapidly with radius unlike those of the model with the potential well. Although we use the Plummer model as the initial model, the anisotropy parameter is likely to be similar to that of the isochrone model as shown in Quinlan et al. (1995). However, the maximum anisotropy is located at the larger radius than  $r_{\text{inf}}$ . On the other hand, for the Model 4, the radial velocity dispersion is enhanced due to the radial acceleration from the external potential as mentioned in the previous section. Obviously this is an artifact of the fixed external potential. If the external potential is a live one, the velocity dispersion and the anisotropy would be more smooth. However, as we will see in the following section, the details of the velocity profiles and anisotropy would not affect on the estimation of binaries as the binary formation rate at the outer part becomes very low.

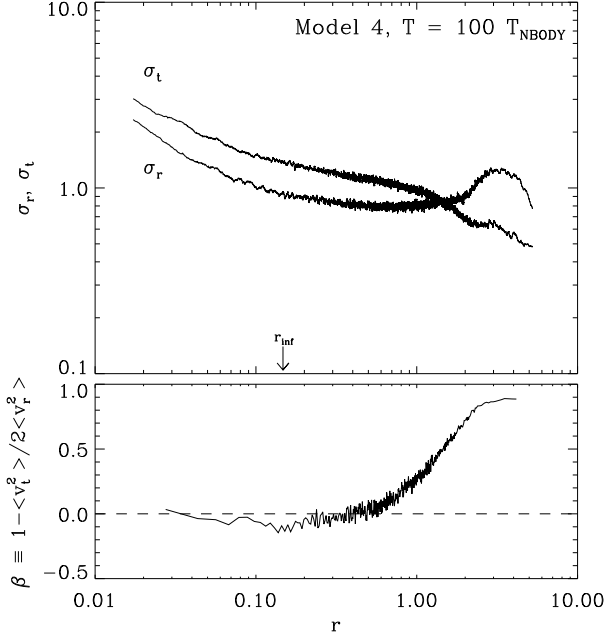


**Figure 8.** Profiles of Radial and tangential velocity dispersion (upper) and the anisotropy parameter (lower) for Model 4 with the external Plummer potential. For the inner region, the velocity distribution is similar to that of isolated models. However, the tangential anisotropy is driven by the external potential well at the outer region.

## 5 BLACK HOLE BINARIES

### 5.1 Close encounters and GR capture

In order to estimate the merger and detection rates of BH-BH binary coalescences, we need to know binary formation rates as well as the orbital parameter distribution just after the capture. We only consider the direct capture by gravitational radiation during close encounters.

The energy loss and change of orbits by GW for binary systems were first studied by Peters & Mathews (1963) based on the post-Newtonian (PN) approximation. Later, Hansen (1972) extended the study of Peters & Mathews (1963) to the hyperbolic encounters. With given masses  $m_1, m_2$ , a semi-major axis  $a$  (defined as  $a = Gm_1m_2/2E_0$  where  $E_0$  is the initial orbital energy) and an eccentricity  $e$ , the energy and orbital angular momentum losses by GR are given by

$$\Delta E = -\frac{2}{15} \frac{G^{7/2}}{c^5} \frac{m_1^2 m_2^2 (m_1 + m_2)^{1/2}}{a^{7/2} (e^2 - 1)^{7/2}} \times \left[ (\pi - \theta_0)(96 + 292e^2 + 37e^4) + \frac{1}{3} e \sin \theta_0 (602 + 457e^2) \right], \quad (10)$$

$$\Delta L_z = -\frac{8}{5} \frac{G^3}{c^5} \frac{m_1^2 m_2^2}{a^2 (e^2 - 1)^2} \left[ (\pi - \theta_0)(8 + 7e^2) + e \sin \theta_0 (13 + e^2) \right] \quad (11)$$

where  $G, c$  and  $\theta_0$  are gravitational constant, speed of light and the incidence angle at infinity defined as  $\theta_0 = \cos^{-1}(1/e)$ , respectively. Two encountering but unbound stars, therefore, become a binary if the energy loss by GR is larger than the orbital energy  $E_0$ .

From equations (10) and (11), one can obtain the semi-major axis and the eccentricity of the captured binary as

$$a' = -\frac{Gm_1m_2}{2(E_0 + \Delta E)} \quad (12)$$

$$e' = \sqrt{1 - \frac{(m_1 + m_2)(L_{z,0} + \Delta L_z)}{Gm_1^2m_2^2a'}} \quad (13)$$

where the subscript 0 indicates the initial value.

Many previous studies have discussed the GR captures of compact stars in dense stellar systems (e.g., Quinlan & Shapiro 1987, 1989; O'Leary et al. 2009). The starting point is the cross section for GR capture. Quinlan & Shapiro (1987) deduced the capture cross section under the parabolic approximation. This approximation is valid because trajectories of the stars near the pericentre, where bulk of the GWs is radiated, are almost identical to parabolic with the same pericentre distance. The equation (10) is rewritten with parabolic approximation as

$$\Delta E = -\frac{85\pi}{12\sqrt{2}} \frac{G^{7/2}}{c^5} \frac{m_1^2 m_2^2 (m_1 + m_2)^{1/2}}{r_p^{7/2}} \quad (14)$$

where  $r_p$  is the pericentre distance. Again, the GR capture will happen when the energy loss is larger than the orbital energy. By the requirement of  $|\Delta E| > m_1m_2v_\infty^2/2(m_1+m_2)$ , Quinlan & Shapiro (1989) obtained the maximum pericentre distance for GR capture:

$$r_{p,\text{max}} = \left[ \frac{85\pi\sqrt{2}}{12} \frac{G^{7/2}}{c^5} \frac{m_1m_2(m_1+m_2)^{3/2}}{v_\infty^2} \right]^{2/7} \quad (15)$$

where  $v_\infty$  is the relative velocity at infinity. Therefore, the capture cross section is given as

$$\Sigma_{\text{cap}} = \pi r_{p,\text{max}}^2 \left[ 1 + \frac{2G(m_1+m_2)}{r_{p,\text{max}}v_\infty^2} \right] \simeq 17 \frac{G^2 m_1 m_2 \eta^{-5/7}}{c^{10/7} v_\infty^{18/7}} \quad (16)$$

where  $\eta$  is the symmetric mass ratio defined as  $\eta \equiv m_1m_2/(m_1+m_2)^2$ . We assumed that gravitational focusing is dominant compared to the geometrical cross section for the last equality in the above equation.

Here, we are going to introduce a statistical interpretation of GR captures to understand the situations and predict the BH-BH binary coalescences in realistic regime. We can assume that the motions of stars follow the one-dimensional normal distribution with a given velocity dispersion  $\sigma$ . From the equation (16), the distribution of the pericentre distance of encountering stars also becomes uniform (i.e.,  $dS = d(\pi b^2) \simeq 2\pi G(m_1+m_2)/v_\infty^2 \cdot dr_p$ ) if the gravitational focusing dominates. Therefore, for unbound close encounters that lead to the formation of binaries by GR,  $r_p/r_{p,\text{max}}$  is distributed uniformly in the range  $[0, 1]$ . Under the parabolic approximation, the semi-major axis and the eccentricity can be rewritten with  $\sigma$  and  $r_p/r_{p,\text{max}}$  from the equations (14) and (15) as

$$a = \frac{GM}{2\sigma^2} \approx 1.58\text{AU} \left( \frac{M}{20M_\odot} \right) \left( \frac{\sigma}{75\text{km/s}} \right)^{-2}, \quad (17)$$

$$e = 1 + \left( \frac{170\pi\eta}{3} \right)^{2/7} \left( \frac{\sigma}{c} \right)^{10/7} \left( \frac{r_p}{r_{p,\text{max}}} \right) \approx 1 + 1.57 \times 10^{-5} \eta^{2/7} \left( \frac{\sigma}{75\text{km/s}} \right)^{10/7} \quad (18)$$

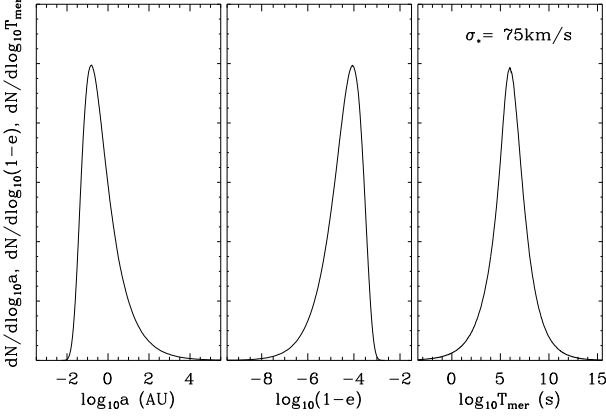


**Figure 9.** Distribution of semi-major axis (left panel), eccentricity (middle panel) and merging time (right panel) for  $10M_{\odot}$  BH-BH binaries in the Milky-Way-like galaxies (i.e.,  $\sigma = 75$  km/s).

where  $M$  is the sum of masses, and we set  $v_{\text{inf}} = \sqrt{2}\sigma$ . By assuming  $r_p/r_{p,\text{max}} = 1/2$  typical pericentre distance for GR capture of encountering two  $10M_{\odot}$  BHs is 2514km, corresponding to about  $840 R_{\text{Sch}}$  (Schwarzschild radius), in Milky-Way-like galaxies (i.e.,  $\sigma = 75$  km/s). Because the pericentre distance is nearly the same before and after capture, the semi-major axis and eccentricity of the binary formed by GR capture are given by

$$a' = a \left[ \left( \frac{r_p}{r_{p,\text{max}}} \right)^{-7/2} - 1 \right]^{-1} \approx 0.153 \text{AU} \left( \frac{M}{20M_{\odot}} \right) \left( \frac{\sigma}{75 \text{km/s}} \right)^{-2}, \quad (19)$$

$$e' = 1 - \frac{a}{a'}(e - 1) \approx 1 - 1.62 \times 10^{-4} \eta^{2/7} \left( \frac{\sigma}{75 \text{km/s}} \right)^{10/7}. \quad (20)$$

For the case with velocity dispersion of  $\sigma \sim 75$  km/s, the eccentricity of a typical binary formed by GR capture is  $1 - e' \sim 10^{-4}$ . From the distribution of semi-major axis and eccentricity, we can determine the distribution of merging time for such binaries. The merging time is given by (Peters 1964)

$$T_{\text{mer}} = \frac{5}{64} \frac{c^5 a_0^4 (1 - e_0^2)^{7/2}}{G^3 m_1 m_2 (m_1 + m_2)} \left\{ 1 + \frac{73}{24} e_0^2 + \frac{37}{96} e_0^4 \right\}^{-1} \quad (21)$$

where  $a_0$  and  $e_0$  are the initial semi-major axis and eccentricity, respectively. Since the orbits of binaries in our consideration are nearly parabolic, the merging time has a strong dependence on the velocity dispersion, i.e.,  $T_{\text{mer}} \approx a_0^4 (1 - e_0)^{7/2} \approx \sigma^{-3}$ . Note that this merging time is not corrected for lower order PN terms (see §7 and Appendix A for other PN corrections). In Fig. 9, we have shown the distribution of semi-major axis, eccentricity and merging time of BH-BH binaries from equations (19), (20) and (21). As mentioned, we assume that the velocity of star follows one-dimensional normal distribution with  $\sigma = 75$  km/s (i.e., the velocity dispersion for the Milky Way) and the pericentre distance  $r_p/r_{p,\text{max}}$  follows uniform distribution. The peak position of each distribution is equivalent to the typical value in equations (19) and (20). For merging time, the mode is  $\sim 10^6$  second. Although the

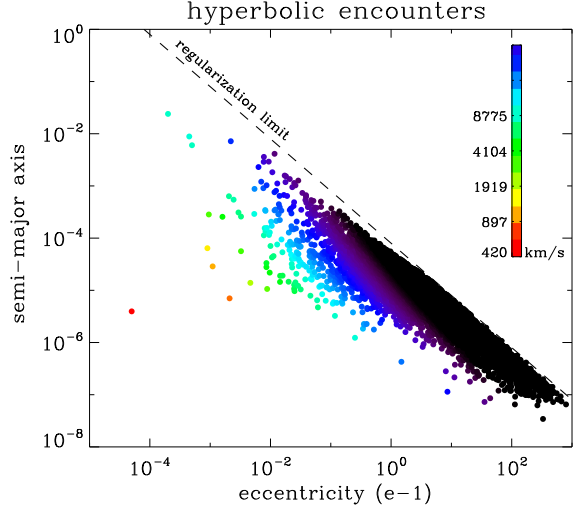


**Figure 10.** Distribution of semi-major axis and eccentricity of GR captured binaries for the Model 4. Different colors mean the velocity dispersion at the radius of influence in physical units as indicated by the color bar. These encountering stars become binaries by GR capture.

distribution is quite wide, almost all binaries will merge within a few thousand years.

## 5.2 Merger rates

We collect the parameters of all close encounter events in our simulations in order to investigate the GR capture and the compact binary coalescences. In the NBODY6 code, the regularization algorithm helps the calculation of very close orbits with high precision. If the separation or the time step of stars becomes smaller than certain criteria, the stars are taken away from the main loop, and their motions are calculated with time smoothing. We turn on the KS regularization, the two-body regularization scheme, and extract the semi-major axes and the eccentricities of pairs experiencing close encounters at the pericentre passage to avoid the effect of perturbation by nearby stars. We have shown an example of  $(a, e)$  distribution of the close hyperbolic encounters for the Model 4 after  $T > t_{\text{MBH}}$  in Fig 10. Each filled dot represents each encounter and the dashed line shows the limit of KS regularization (i.e.,  $r_{\text{peri}} \sim 10^{-4}$ ), so pairs lying above this line are not considered in our investigation. In order to determine whether a certain encounter results in a binary, we therefore need to convert our dimensionless results to physical quantities according to the equation (5). In Fig. 10, there are some orbits with rainbow colors. These colored orbits will become binaries when the overall velocity dispersion of stellar system is larger than that velocity (e.g., the orbit colored red at the left-end will become a binary when the velocity dispersion is  $\sim 400$  km/s). By counting the number of capture events, we estimate the binary formation rates in our simulations.

For a single BH passing through stars with a speed  $v$ , the time scale for GR capture is

$$t_{\text{cap}} \equiv (\Sigma_{\text{cap}} n v)^{-1} \quad (22)$$

where  $n$  is the number density of background stars. The binary formation rate between stars with different mass  $m_1$  and  $m_2$  in the shell with the range  $[r, r + dr]$  can be expressed as

$$\frac{d\Gamma_{\text{cap}}}{dr} = 4\pi r^2 n_1(r) n_2(r) \langle \Sigma_{\text{cap}} v \rangle \quad (23)$$



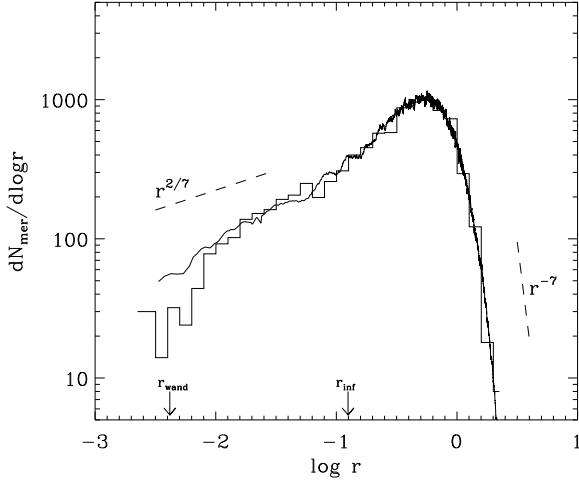


**Figure 11.** Radial distribution of GR binary capture rates. The solid curve is the semi-analytic model from the equation (25). This semi-analytic model agrees well with events in the simulation except for the inner region. From the theoretical models, the slope of distribution inside the radius of influence is expected to be  $2/7$ . Although the actual slope differs from the theoretical models due to the overall incompleteness of Bahcall-Wolf cusp as shown in Fig. 6, the contribution to the overall merger rate within this radius is small. Thus, it does not significantly affect the estimation of the entire merger rates.

where  $\langle \Sigma_{\text{cap}} v \rangle$  is the velocity averaged value. Thus, assuming  $v_\infty = \sqrt{2}v$  in equation (16) and replacing  $v$  by  $\sigma(r)$ , the velocity dispersion, we have

$$\frac{d\Gamma_{\text{cap}}}{dr} \simeq 87 \frac{G^2 m_1 m_2 \eta^{-5/7}}{c^{10/7}} r^2 n_1(r) n_2(r) \sigma(r)^{-11/7}. \quad (24)$$

For the case of systems composed identical stars,  $m = m_1 = m_2$ , this equation becomes

$$\frac{d\Gamma_{\text{cap}}}{dr} \simeq \frac{1}{2} 87 \frac{G^2 m^2 (1/4)^{-5/7}}{c^{10/7}} r^2 n^2(r) \sigma(r)^{-11/7} \quad (25)$$

where the half is to avoid double counting and  $\eta = 1/4$ . Fig. 11 shows the radial distribution of cumulative capture events  $dN_{\text{cap}}/d \log r$  during  $\Delta t = 2000 T_{\text{NBODY}}$ . Histogram is from  $N$ -body simulations of Model 4, and the noisy line is from the equation (25) (i.e.,  $dN_{\text{cap}}/d \log r = r d\Gamma_{\text{cap}}/dr \cdot \Delta t$ ) with the density and the velocity dispersion profiles from Figs. 3 and 4, respectively. In order to get large sample size, we set the unit of velocity to the half of the speed of light ( $0.5c$ ). Although this velocity is unrealistically high, it is possible to guess what happens in realistic situations because there is no relativistic effect on the simulations. The simulation results and our semi-analytic model from given density and velocity dispersion profiles show good agreement at the radius larger than  $r_{\text{inf}}$ . However, at  $r < r_{\text{inf}}$ , there is some discrepancy between them: the binary formation rate obtained with simulation is smaller than that with the equation (25). One possible reason is the time variation of density structure within the radius of influence as shown in Fig. 6. From the theoretical model of star distribution within the radius of influence (e.g.,  $\rho(r) \sim r^{-7/4}$  and  $\sigma(r) \sim r^{-1/2}$ ), we obtain the slope of  $dN_{\text{cap}}/d \log r$  as

$$\frac{dN_{\text{cap}}}{d \log r} \propto r^{2/7}. \quad (26)$$

However, the slope inside  $r_{\text{inf}}$  in Fig. 11 is not the same as  $\frac{2}{7}$  because of the incompleteness of the Bahcall-Wolf cusp (see Fig.

6). Around the wandering radius, even merger events from  $N$ -body simulations and the semi-analytic model show disagreement. This gap is likely due to escapers that cause indirect heating at that radius. Incidentally, more than 80 per cent of events occurred outside  $r_{\text{inf}}$ , and the peak of  $dN_{\text{cap}}/d \log r$  is located at  $r_{\text{half}}$ . The fact that the most of the merger takes place outside the radius of influence is mainly because the density distribution follows Bahcall-Wolf or shallower. Our results are quite different from O’Leary et al. (2009) who found that the merger rate is more centrally concentrated because the distribution of the black holes is much steeper than Bahcall-Wolf due to the mass segregation (see Fig. 7 of O’Leary et al. 2009). Our simulation is one component, and thus cannot reproduce the effect of the mass segregation. We note here that many recent simulations with different approaches showed that the density profile of the massive component follows the Bahcall-Wolf or steeper while lower mass component follows shallower slope (direct  $N$ -body simulations, Baumgardt et al. 2004b) (Monte-Carlo simulations, Freitag et al. 2006) and (time-dependent Fokker-Planck equation, Fiestas et al., in preparation). If that is the case, the small discrepancy of analytical estimation at small radii thus does not affect the estimation of the total capture rates.

In order to obtain the overall merger rate for NC, we need to integrate the equation (25) over the volume. We can assume that the merger rate is equivalent to the capture rate because the merging time of BH-BH binary in our simulations is negligible compared to the cluster time scales as discussed before. It is difficult to estimate the merger rate because  $n(r)$  and  $\sigma(r)$  are not simple function of  $r$ . Assuming that the velocity dispersion remains a constant over the entire cluster, and replacing the integral  $\int n^2 r^2 dr$  by  $N \tilde{n}$ , we can write the integrated merger rate as

$$\begin{aligned} \Gamma_{\text{mer}} &\approx m^2 \cdot N \cdot \tilde{n} \cdot \sigma_*^{-11/7} \\ &\sim M^{-1} \cdot \sigma_*^{31/7} \end{aligned} \quad (27)$$

where  $\tilde{n}$ ,  $\sigma_*$  and  $M$  are mean number density, the velocity dispersion of the system and total mass of the cluster, respectively. We have used the virial theorem to get the last relationship. We see that the event rate is inversely proportional to the total mass of the cluster with rather steep dependence on the velocity dispersion of the cluster. To convert our results to physical units, it is necessary to determine the representative value of velocity dispersion of  $N$ -body simulations. We already estimated the density-weighted velocity dispersion in equation (7) as similar to the observational estimation of velocity dispersion of bulge as (McConnell & Ma 2013). Note that the effective radius of bulge that is the upper limit of the integration for the systemic velocity dispersion in observations is much larger than the half-mass radius of NCs. According to recent observation for the calibration of velocity dispersion of nearby galaxies (Kang et al. 2013), however, the velocity dispersion does not change much with the aperture size. Thus, the velocity dispersion of NCs is nearly identical to that of bulges.

Figs. 12 and 13 show the merger rates as a function of the velocity dispersion in the physical unit. The mass ratio of MBH to the cluster is fixed at 0.2 for Fig. 12 ( $\sigma_* \sim 0.79$ ) and 0.1 for Fig. 13 ( $\sigma_* \sim 0.75$ ), respectively. Different symbols represent the different models with different  $N$  and dashed lines are from the time averaged result of numerical integration of the equation (27). Because of the limitations in the number of particles and the integration time, we only consider the unrealistic range of the velocity dispersion ( $1,000 \text{ km/s} < \sigma_* < 20,000 \text{ km/s}$ ). Nevertheless, because

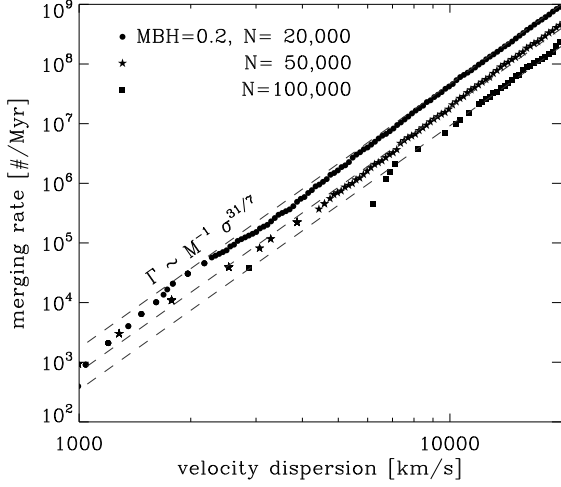


**Figure 12.** Merger rates as a function of velocity dispersion for models 2-4. The MBH mass is 20% of the total mass of the cluster. Filled symbols are from the number counts in simulations with different number of stars. Dashed lines show the equation (27) with the proportional constants obtained from the simulations. There are good correlations between merger rates and velocity dispersion.

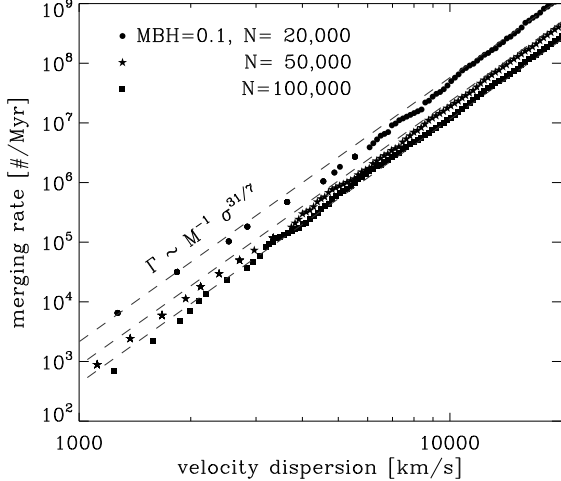


**Figure 13.** Merger rates as a function of velocity dispersion for models 5-7. The MBH mass is 10% of the total mass of the cluster.

the results show very good scaling relation with the velocity dispersion and the total mass of the cluster as predicted by the equation (27), it is possible to extrapolate our results to realistic parameters for NC. As a result, the merger rate can be expressed by an equation with the mass of MBH and the velocity dispersion:

$$\Gamma_{\text{mer}} \approx 2.06 \times 10^{-4} \text{Myr}^{-1} \left( \frac{M_{\text{MBH}}}{3.5 \times 10^6 M_{\odot}} \right)^{-1} \left( \frac{\sigma_*}{75 \text{km/s}} \right)^{31/7}$$

for  $M_{\text{MBH}} = 0.2 M_{\text{tot}}$ , (28)

$$\Gamma_{\text{mer}} \approx 8.58 \times 10^{-5} \text{Myr}^{-1} \left( \frac{M_{\text{MBH}}}{3.5 \times 10^6 M_{\odot}} \right)^{-1} \left( \frac{\sigma_*}{75 \text{km/s}} \right)^{31/7}$$

for  $M_{\text{MBH}} = 0.1 M_{\text{tot}}$ . (29)

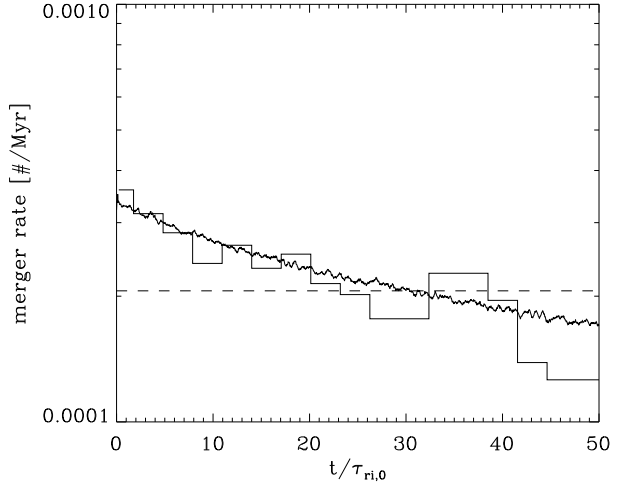


**Figure 14.** Time evolution of merger rate from Model 2 as a function of time at the radius of influence. The merger rate is scaled for a Milky-Way-like galaxy. Noisy line and histogram are from the integration of equation (25) and the number of events counted in the simulations, respectively. Due to the cluster expansion, the merger rate decreases with time. The dashed horizontal line represents the merger rate from equation (28).

Thus, the merger rate is about  $2.06 \times 10^{-10} \text{yr}^{-1}$  for Milky-Way-like galaxies if we assume that the total mass of embedded star cluster is 5 times heavier than the MBH.

Our realization of the NC is not static: the NCs expand slowly with time even though they are bounded by the external potential as described in §4. The time evolution of the merger rate for a Milky-Way-like galaxy is represented in Fig. 14, which is estimated from the Model 2 with  $N = 20,000$  in order to see the long-term evolution. The time is scaled by the initial relaxation time at the radius of influence  $\tau_{\text{ri},0}$  (Spitzer 1987) after growth of the MBH

$$\tau_{\text{ri},0} \equiv \frac{\langle v^2 \rangle^{3/2}}{15.4 G^2 \bar{m} \bar{\rho}_{\text{inf}} \ln \Lambda} \quad (30)$$

where  $\bar{m}$  and  $\bar{\rho}_{\text{inf}}$  are the mean mass (for equal-mass,  $\bar{m} = M/N$ ) and the mean density inside the radius of influence, respectively. The noisy line is the merger rate from the numerical integration of the equation (25). For comparison, we plot the histogram showing the number of events counted in the simulation. They are selected with  $\sigma_* = 10^4 \text{km/s}$  for sufficient samples and rescaled to  $\sigma_* = 75 \text{km/s}$  range. The horizontal dashed line is the time-averaged merger rate in equation (28). Due to the expansion of the cluster, the merger rate decreases with time. These two estimates show good agreement, and therefore it is possible to surmise the merger rates from given density and velocity structures of stellar systems. The conversion of these merger rates to the detection rates for GW detectors will be presented in next section.

## 6 DETECTION RATES OF BH BINARY MERGERS

To determine the detection rate of GWs from BH-BH binary coalescences for GW detectors, it is necessary to calculate how many events occur per unit volume in the universe and horizon distance of GW detectors. In the previous section, we estimated the merger rates in NC as a function of the mass of MBH and the velocity dispersion. It is well known that there is a good correlation between

the mass of MBH and the velocity dispersion of surrounding stars (e.g., Tremaine et al. 2002)

$$M_{\text{MBH}} \approx 1.3 \times 10^8 M_{\odot} (\sigma_*/200 \text{ km s}^{-1})^4 \quad (31)$$

in a range of the mass of MBH [ $10^6 M_{\odot}$ ,  $10^9 M_{\odot}$ ]. Later, Barth et al. (2005) confirmed that the relation is also valid for MBHs down to  $10^5 M_{\odot}$ . The merger rate for a NC, therefore, has a weak dependence on the mass of central MBH  $\Gamma \sim M_{\text{MBH}}^{3/28}$  (O’Leary et al. 2009), and the merger rates of (28) and (29) become

$$\Gamma_{\text{mer}} \approx 3.33 \times 10^{-4} \text{ Myr}^{-1} \left( \frac{M_{\text{MBH}}}{3.5 \times 10^6 M_{\odot}} \right)^{3/28} \quad (32)$$

for  $M_{\text{MBH}} = 0.2 M_{\text{tot}}$ ,

$$\Gamma_{\text{mer}} \approx 1.39 \times 10^{-4} \text{ Myr}^{-1} \left( \frac{M_{\text{MBH}}}{3.5 \times 10^6 M_{\odot}} \right)^{3/28} \quad (33)$$

for  $M_{\text{MBH}} = 0.1 M_{\text{tot}}$ .

However, there are several factors that give rise to uncertainties in merger rates. From the equation (24), we can infer that the merger rate is proportional to the total mass of different mass components  $M_1$  and  $M_2$ . As we mentioned before, however, we assumed that all stars are  $10 M_{\odot}$  BHs. There exist other stellar objects such as MS stars, white dwarfs (WDs), NSs and BHs in real stellar systems. Hopman & Alexander (2006) have studied the effect of mass segregation of stars around a MBH and concluded that the number fraction of different stellar objects evolves from the initial state (i.e.,  $N_{\text{MS}} : N_{\text{WD}} : N_{\text{NS}} : N_{\text{BH}} = 1 : 0.1 : 0.01 : 10^{-3}$ , for continuously star-forming populations; Alexander 2005) to  $N_{\text{MS}} : N_{\text{WD}} : N_{\text{NS}} : N_{\text{BH}} = 1 : 0.09 : 0.012 : 0.06$  within 0.1 parsec for Milky-Way-like galaxies. If we set the mass of MS stars ( $0.7 M_{\odot}$ ), WDs ( $0.6 M_{\odot}$ ) and NSs ( $1.4 M_{\odot}$ ), the mass fraction of BHs  $\mathcal{M}_{\text{BH}}$  is about 44 per cent of the total mass. When we simply assume that the merger rate of BHs in galactic nuclei can be expressed by the equations (32) and (33) with multiplication of  $\mathcal{M}_{\text{BH}}^2$ , the merger rate in equation (32) is reduced to  $6.45 \times 10^{-11} \text{ yr}^{-1}$ , which is about 3 times smaller than the estimation of O’Leary et al. (2009) for BHs with similar mass ranges. Of course, it is more complicated to correct for the mass function rather than our consideration because the mass fraction of BHs varies with the radius. Furthermore, the mass fraction in our consideration is adequate for innermost region although the capture events happen most frequently around the half-mass radii as shown in Fig. 11. The mass fraction of BHs around the half-mass radius might be smaller than that from Hopman & Alexander (2006), and thus, our results could be an overestimation.

As discussed earlier, our model is one component, and the effect of the density profiles around the central black hole may not be correct. If the density profile of the massive component is steeper significantly for massive components, the merger rate could be enhanced (O’Leary et al. 2009). Moreover O’Leary et al. (2009) have shown that using different mass spectra of stellar mass BHs can affect not only the merger rates by a factor of  $\sim 2$  but also the detection rates by a factor of  $\sim 10$ . In that sense our result could be an underestimation. However, as we mentioned, Fiestas et al. (in preparation) found that the density profile of BHs does not significantly deviate from that of dominant components (low mass stars) from time-dependent Fokker-Planck simulations.

The dynamical evolution of NCs also affects the merger rates. The merger rate varies at most by a factor of  $\sim 2$  from  $T = 0$  to

$T = 200 \tau_{\text{ri},0}$  as shown in Fig. 14. Merritt et al. (2007) have estimated the relaxation times  $\tau_{\text{ri},0}$  for ACS Virgo samples of galaxies observed by Côté et al. (2004), and found the relation between the relaxation time and the central velocity dispersion. According to the relation,  $\tau_{\text{ri},0}$  is less than a Hubble time with smaller velocity dispersion than 100 km/s, corresponding to  $M_{\text{MBH}} \sim 1.6 \times 10^7 M_{\odot}$ . Therefore, the merger rates for NCs with smaller MBHs can be affected by the dynamical evolution. In addition, the relaxation time of galactic nuclei implies that most of NCs with larger MBHs do not contribute to the merger rates as much as those with smaller MBHs because the number fraction of BHs in relaxed nuclei is several tens of times larger than that of initial conditions due to the mass segregation (Hopman & Alexander 2006), and the merger rate weakly depends on the mass of central MBH (O’Leary et al. 2009). O’Leary et al. (2009) also noted that the variance of the number density of galactic nuclei can affect the merger rate. They have estimated the variance of the number density from the results of Merritt et al. (2007) and found that the merger rate is enlarged as much with the rescale factor  $\xi \sim 10 - 100$ . However, see Tsang (2013), for possible reduction of the rescale factor by about a factor of 5.

In order to calculate the merger rate per unit cosmological volume, we convolve the merger rate per NC with the number density of MBHs in the universe (for more details, see §3.3.5 of O’Leary et al. 2009). Aller & Richstone (2002) determined the number density of MBHs from the luminosity function of galaxies as

$$\frac{dn_{\text{MBH}}}{dM_{\text{MBH}}} = c_{\bullet} \left( \frac{M_{\text{MBH}}}{M_{\bullet}} \right)^{-\alpha} e^{-M_{\text{MBH}}/M_{\bullet}} \quad (34)$$

with the best fitting parameters of  $(c_{\bullet}, M_{\bullet}, \alpha) = (3.2 \times 10^{-11} M_{\odot}^{-1} \text{ Mpc}^{-3}, 1.3 \times 10^8 M_{\odot}, 1.25)$ . Note that using the MBH mass function of Aller & Richstone (2002) can lead to an overestimation of the detection rates at least by a factor of 2, especially at the low mass range of MBHs (Graham & Driver 2007). The merger rate per volume, therefore, is obtained by integrating the rate over the SMBH mass distribution

$$\mathcal{R}_{\text{mer}} = \int_{M_1}^{M_u} \Gamma_{\text{mer}}(M_{\text{MBH}}) \xi \frac{dn_{\text{MBH}}}{dM_{\text{MBH}}} dM_{\text{MBH}} \quad (35)$$

where  $M_u$  and  $M_1$  are the upper and lower limits for integration, and  $\Gamma_{\text{m,gal}}$  and  $\xi$  are the merger rate per galaxy as a function of the mass of MBH and the scale factor for number density variance, respectively. The upper limit can be fixed to  $M_{\text{MBH}} \sim 10^7 M_{\odot}$  by the time scale requirement as discussed above. However, we still do not have the exact lower limit of the MBH mass, which is currently about  $10^5 M_{\odot}$  from the observation of Barth et al. (2005). By taking the lower limit of the MBH mass to  $10^4 M_{\odot}$ , the equation (35) gives us the merger rate density

$$\mathcal{R}_{\text{mer}} \approx 3.1 \Gamma_{\text{mer,MW}} \xi_{30} \text{ Mpc}^{-3} \quad (36)$$

where  $\Gamma_{\text{mer,MW}}$  is the merger rate for a Milky-Way-like galaxy, and  $\xi_{30}$  is the rescale factor for the variance of the number density of stars normalized by 30 (i.e.,  $1/3 \leq \xi_{30} \leq 10/3$ ; O’Leary et al. 2009). Choosing different lower limit of the MBH mass from  $10^3 M_{\odot}$  to  $10^5 M_{\odot}$  will give us an uncertainty by a factor of  $\sim 3$  in the merger rate density.

Now, we can estimate the detection rate of BH-BH binary coalescences by next generation GW detectors. By assuming that the merger events occur uniformly in the universe, the detection rate only depends on the size of cosmological volume which we can cover and can be expressed by (O’Leary et al. 2006;

Belczynski et al. 2007; Downing et al. 2011; Bae et al. 2014)

$$\mathcal{R}_{\text{det}} = \mathcal{R}_{\text{mer}} \int \frac{4\pi r(z)^2}{1+z} \frac{dr}{dz} dz \quad (37)$$

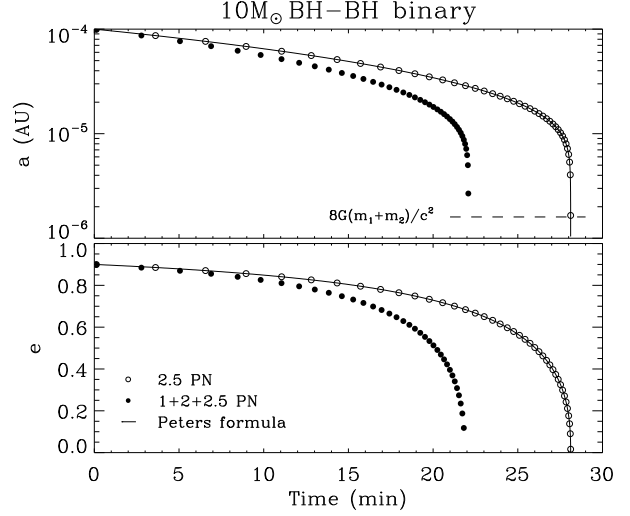
where  $z$  is the cosmological redshift, and the factor of  $(1+z)^{-1}$  represents the cosmological time dilation. For existing GW detectors, the effect of redshift can be negligible because their coverage is not too far (i.e., the horizon distance  $D_h$  are 33 Mpc for NS-NS binaries and 161 Mpc for BH-BH binaries corresponding to  $z \sim 0.01$  and 0.04 in standard  $\Lambda$ CDM cosmology, respectively; Abadie et al. 2010). However, for next generation GW detectors, the effect of redshift becomes important, especially for BH-BH binaries. The maximum horizon distance  $D_h$  can be obtained from signal-to-noise ratio (SNR) of GW signals (for more details, see §4.2 of O’Leary et al. 2009). Because the redshift affects both the mass of source and the frequency, SNR should be estimated from the waveforms carefully. Only few studies (Baker et al. 2007; O’Leary et al. 2009; Reisswig et al. 2009) have estimated  $D_h$  for BH-BH binaries for given SNR.

Table 2 shows the detection rates expected for advanced LIGO. Because we mainly considered the equal-mass models for only BHs, the detection rates are corrected by the factor of  $\mathcal{M}_{\text{BH}}^2$ . We estimated detection rates by using  $D_h$  from different studies (Baker et al. 2007; Reisswig et al. 2009; Abadie et al. 2010). All  $D_h$ s are corrected for the orientation of sources. Note that  $D_h$  from Abadie et al. (2010) does not include the cosmological effect of the redshift.  $D_h$  from Reisswig et al. (2009) is for spinning BHs but independent of the spin of BHs for  $10M_\odot$  BHs. We list three detection rates  $\mathcal{R}_{\text{det},l}$ ,  $\mathcal{R}_{\text{det},re}$  and  $\mathcal{R}_{\text{det},h}$  in Table 2 for different models and different estimates of detection horizon ( $D_h$ ). We first calculated the ‘reasonable’ expected detection rate  $\mathcal{R}_{\text{det},re}$  using the merger rate given in equation (36). Given several uncertainties including the variance of the number density, dynamical evolution and the lower limits of the MBH, we assume that the total range of uncertainty is a factor of 60. Thus ‘low’ expected rate  $\mathcal{R}_{\text{det},l}$  is simply obtained by dividing  $\mathcal{R}_{\text{det},re}$  by  $\sqrt{60}$  while the ‘high’ expected rate  $\mathcal{R}_{\text{det},h}$  is calculated by multiplying the same factor. The whole range of the expected detection rate lies between 0.02  $\sim$  14  $\text{yr}^{-1}$  depending on the maximum horizon distance and uncertainties. These estimates are able to cover those of O’Leary et al. (2009) (5-20  $\text{yr}^{-1}$ ) for BHs around  $10M_\odot$  although the lowest value is quite smaller than that.

Our estimations have some limitations; (1) We ignore the initial mass function. This mass function may affect not only the evolution of systems by the relaxation between mass components but also the merger rates for BHs with different masses. (2) We need to consider various range of  $M_{\text{MBH}}/M_{\text{cl}}$  (e.g., Graham & Spitler 2009, suggested that there is a rough relation between the mass of MBH and NC.) (3) The exact calculation for SNR is necessary in order to obtain more reasonable detection rates. We considered the mass segregation and its effect only approximately. These limitations would be considered in future works.

## 7 BLACK HOLE BINARY COALESCENCE AND WAVEFORM

Solving Einstein field equation exactly is very difficult and has only been done numerically. Fortunately, during inspiral phase of compact binary coalescences, the Einstein equation can be simplified with the PN expansion. When a compact binary is formed, the orbit decays with time due to the GR. The orbit-averaged change of



**Figure 15.** Time evolution of semi-major axis and eccentricity of a coalescing binary. Solid line is from the integration of Peters formula. Open and filled circles are the results of simulations with 2.5PN correction only and full PN correction, respectively. The simulation with 2.5PN correction only agrees well with Peters formula while that with full PN correction significantly festinates compared to Peters formula.

the semi-major axis and the eccentricity by GR is first derived by Peters (1964) as

$$\left\langle \frac{da}{dt} \right\rangle = -\frac{64}{5} \frac{G^3 m_1 m_2 (m_1 + m_2)}{c^5 a^3 (1 - e^2)^{7/2}} \left( 1 + \frac{73}{24} e^2 + \frac{37}{96} e^4 \right), \quad (38)$$

$$\left\langle \frac{de}{dt} \right\rangle = -\frac{304}{15} e \frac{G^3 m_1 m_2 (m_1 + m_2)}{c^5 a^4 (1 - e^2)^{5/2}} \left( 1 + \frac{121}{304} e^2 \right) \quad (39)$$

in the 2.5PN order ( $\sim 1/c^5$ , the first order GR term). However, the orbital evolution is also affected by other PN order terms such as 1PN (relativistic precession), 1.5PN (spin-orbit coupling), 2PN (spin-spin coupling, high order relativistic precession) and higher orders. With full consideration of PN terms up to 2.5 order, Berentzen et al. (2009) noted that the decay of the binary orbit is much faster than that with 2.5PN only. Although the effect of the spin is quite important for the motions and waveforms of BH-BH binary coalescences, we only consider non-spinning BHs and take 1, 2 and 2.5PN order terms in this study.

The equation of motion with PN correction up to 2.5PN order can be simply written in the centre of mass frame as (Blanchet & Iyer 2003; Mora & Will 2004)

$$\mathbf{a} = \mathbf{a}_n + \mathbf{a}_{\text{pn}} = -\frac{Gm}{r^3} \mathbf{r} + \frac{Gm}{r^2} (A \frac{\mathbf{r}}{r} + B \mathbf{v}) \quad (40)$$

where  $A, B$  are PN coefficients depending on their masses, the relative position  $r$  and relative velocity  $\mathbf{v}$  (see Appendix A, for more details). Many authors have incorporated the PN corrected force in direct  $N$ -body simulations with different PN orders (Lee 1993; Aarseth 2007; Berentzen et al. 2009; Brem et al. 2014). Similarly, we implemented the PN equation of motion to the KS regularization process in NBODY6 code. In the KS regularization process, a two-body motion is sometimes perturbed by other neighboring stars, and these perturbation should be corrected. Thus, we can consider the PN force as a perturbing force in the code by adding the PN force and its time derivative. We designed that the binary will merge when the separation is smaller than four Schwarzschild radii

**Table 2.** Detection rates of BH-BH binaries for advanced LIGO.

| Models | $M_{\text{MBH}}/M_{\text{cl}}$ | $\Gamma_{\text{mer,MW}}$<br>(Myr <sup>-1</sup> ) | $\mathcal{M}_{\text{BH}}^a$ | $D_{\text{h}}$<br>(Mpc) | $\mathcal{R}_{\text{det,l}}^b$<br>(yr <sup>-1</sup> ) | $\mathcal{R}_{\text{det,re}}^c$<br>(yr <sup>-1</sup> ) | $\mathcal{R}_{\text{det,h}}^d$<br>(yr <sup>-1</sup> ) |
|--------|--------------------------------|--|-----------------------------|-------------------------|---|--|---|
| 1-4    | 0.2                            | $3.3 \times 10^{-4}$                             | 0.44                        | 986 <sup>e</sup>        | 0.05  | 0.39   | 3.0   |
|        |                                |  |                             | $\sim 1100^f$           | 0.07  | 0.51   | 4.0   |
|        |                                |  |                             | $\sim 1900^g$           | 0.23  | 1.8  | 14  |
| 5-7    | 0.1                            | $1.4 \times 10^{-4}$                             | 0.44                        | 986 <sup>e</sup>        | 0.02  | 0.16   | 1.3   |
|        |                                |  |                             | $\sim 1100^f$           | 0.03  | 0.21   | 1.7   |
|        |                                |  |                             | $\sim 1900^g$           | 0.10  | 0.74   | 5.7   |

<sup>a</sup>Mean mass fraction of BHs from Hopman & Alexander (2006).

<sup>b,c,d</sup>Low, realistic and high detection rates depending on uncertainties.

<sup>e</sup> $D_{\text{h}}$  with SNR 8 from Abadie et al. (2010) divided by 2.26, the correction factor for sky location and orientation of sources. The effect of redshift is not included.

<sup>f</sup> $D_{\text{h}}$  with SNR 10 from Fig. 16 in Baker et al. (2007).

<sup>g</sup> $D_{\text{h}}$  with SNR 8 from Fig. 3 in Reisswig et al. (2009).

$4R_{\text{Sch}} \equiv 4 \cdot 2G(m_1 + m_2)/c^2$  because the PN approximation is not valid in this regime any more.

For instance, Fig. 15 shows the time evolution of semi-major axis and eccentricity for a  $10M_{\odot}$  BH-BH binary with PN approximation. The initial semi major axis and eccentricity are  $10^{-4}$  AU and 0.9, respectively. The solid line represents the time integration of Peters formula, equations (38) and (39). There is a good agreement between the results of simulation with only 2.5PN term (open circle) and integration of Peters formula. On the other hand, the merging time of simulation with all terms up to 2.5PN (filled circle) is significantly smaller than that of Peters formula as reported in Berentzen et al. (2009). In case of this binary, it takes less than a half hour for merging (i.e.,  $r_{12} \leq 4R_{\text{Sch}}$ ).

In our simulations, most of pairs of close encounters have not been perturbed by other nearby stars. Thus, it is possible to separate the two-body motion with PN correction from the main loop of simulations. We, here, use a TOY<sup>1</sup> code only for a KS two-body motion written by S. J. Aarseth for convenience of exploration of the evolution of merging binaries. The PN implementation mentioned earlier is also adopted in the TOY code. For given semi-major axis and eccentricity, we simulate the orbital evolution of binaries. Fig. 16 shows the merging time of typical BH-BH binaries in equations (19) and (20) with different velocity dispersion of systems. The merging time is estimated by two-body simulations with all PN corrections. A star symbol is showing the result of a galactic nucleus in Milky-Way-like galaxy. In all cases, the merging times are less than a year. Binaries formed by GR capture, therefore, will merge immediately.

The GW waveforms of coalescing binaries have been studied by many authors (e.g., Lincoln & Will 1990; Kidder 1995). As the perturbation of flat-space metric,  $h^{ij}$  in can be expressed by (for more details, see equations 3.21 and 3.22 in Kidder 1995)

$$h^{ij} = \frac{2\mu}{D} \left[ Q^{ij} + P^{0.5} Q^{ij} + P(Q^{ij} + Q_{\text{SO}}^{ij}) + P^{1.5}(Q^{ij} + Q_{\text{SO}}^{ij}) + P^2 Q_{\text{SS}}^{ij} + \dots \right]_{\text{TT}} \quad (41)$$

where  $\mu$  is the reduced mass,  $D$  is the distance from the source

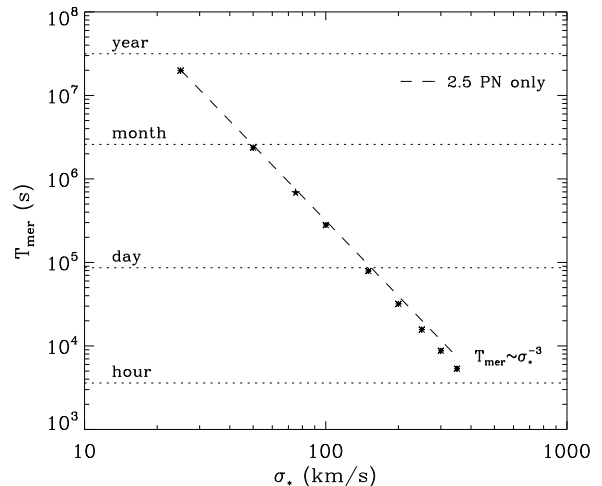


**Figure 16.** Merging time of typical  $10M_{\odot}$  (see §5.1 for details) BH-BH binaries with different velocity dispersion of embedded star clusters. The merging times are obtained from two-body simulations with all corrections up to 2.5PN. The range of velocity dispersion is 50 to 400 km/s, which is correspond to the range of the mass of SMBH from  $5 \times 10^5 M_{\odot}$  to  $2 \times 10^9 M_{\odot}$  according to the  $M_{\text{MBH}} - \sigma_*$  relation from Tremaine et al. (2002). Star symbol represents the binary merging time in the Milky-Way-like galaxies. In all cases, the merging times are smaller than a year.

to the detector,  $Q^{ij}$  is the time derivative of quadrupole moment tensor,  $P^n$  is the PN corrections with order of  $n$ , and SO, SS and TT denote spin-orbit coupling, spin-spin coupling and transverse-traceless gauge, respectively. Here  $G = c = 1$  is used. Since we are interested in the aspects of GW rather than the exact waveforms, we take the leading order of  $h^{ij}$

$$h^{ij} \approx \frac{4\mu}{D} \left[ v^i v^j - \frac{m}{r} n^i n^j \right] \quad (42)$$

with

$$Q^{ij} = 2 \left[ v^i v^j - \frac{m}{r} n^i n^j \right] \quad (43)$$

<sup>1</sup> <http://www.ast.cam.ac.uk/~sverre/web/pages/nbody.htm>

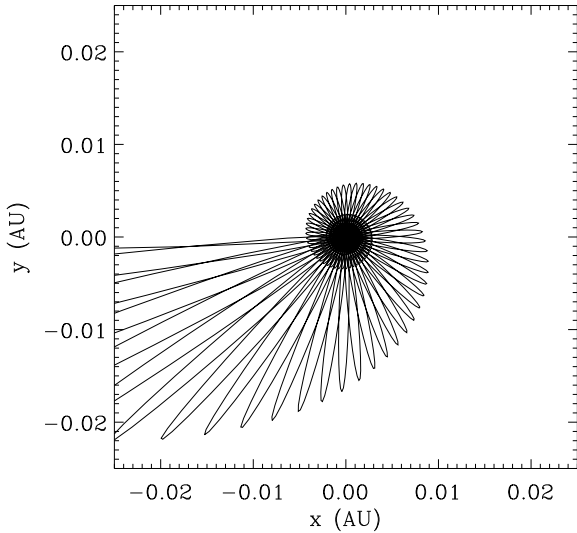


**Figure 17.** Relative orbital motion of a BH-BH binary with the initial semi-major axis 0.153 AU and eccentricity 0.99989, as a representative of typical BH-BH binaries in Milky-Way-like galaxies. The orbits are very eccentric at the beginning. The perihelion is shifted counterclockwise due to the 1PN and 2PN terms, and the orbit shrinks with time due to the GW emission.

where  $v^i$  and  $n^i$  are the relative velocity and the normal vector of the relative position, respectively. It is well known that GWs have two polarization  $+$  and  $\times$  and waveforms are the linear combination of these two polarizations. If we assume that the orbital plane lies on the  $xy$  plane initially in the source coordinate, and the angle between the direction to the detector  $\hat{N}$  and the angular momentum  $\hat{J}$  is  $\Theta$ , the polarizations  $h_+$  and  $h_\times$  are given by (Kidder 1995)

$$h_+ = \frac{1}{2} \left( \cos^2 \Theta h^{xx} - h^{yy} + \sin^2 \Theta h^{zz} - \sin 2\Theta h^{xz} \right), \quad (44)$$

$$h_\times = \cos \Theta h^{xy} - \sin \Theta h^{yz}. \quad (45)$$

Now we provide a waveform of a typical  $10M_\odot$  BH-BH binary coalescence in a Milky-Way-like galaxy for an example. The semi-major axis and eccentricity after GR capture are 0.153 AU and 0.99989 from the equations (19) and (20), respectively. In Fig. 17, the relative motion of BHs on  $xy$  plane is shown. Due to the 1PN and 2PN terms, the position of perihelion is shifted counterclockwise. In addition, by emitting GWs, the orbit shrinks more and more with time. Fig. 18 shows the waveforms for this BH-BH binary coalescence. For simplicity, we assume that the axis of angular momentum is aligned with the direction to the detector (i.e., face-on view,  $\Theta = 0$ ). In Fig. 18(a), the waveform of  $+$  polarization during whole evolution is presented. The merging time is about 8 days. Interestingly, the waveform is burst-like at the beginning, and it takes more than 2 days for the first burst after capture. The detailed waveforms  $h_+$  and  $h_\times$  at this moment are shown in 18(c) and (d). These waveforms are similar to those of eccentric orbits in Abramovici et al. (1992). Fig. 18(b), (e) and (f) show the waveform in the last minute, the detailed view of  $h_+$  and  $h_\times$  a half minute before merging, respectively. In this stage, the orbit is much circularized compared to the beginning, and the orbital frequency is about 10 Hz. At the moment of coalescence, the orbital frequency becomes few hundreds Hz which is the detectable frequency by ground-base GW detectors.

One of the important questions with regards to the GR captured binaries is the typical value of eccentricity when they enter the detectable band of the ground-based detectors. We computed the eccentricity when GW frequency becomes 30 Hz as a function of initial orbital parameters as shown in Fig. 19 using the post-Newtonian approximation with 2.5PN term. The diagonal line is the locus of the typical  $(a_0, e_0)$  plane for different velocity dispersion, and we computed the eccentricities at 30 Hz for up to 10% of peak in probability distribution function along the initial eccentricity for a given velocity dispersion. Different colors represent different eccentricity at 30 Hz. As can be seen from this figure, the GR captured binaries from typical NC with  $\sigma_* \approx 100$  km/sec become nearly circular when they enter the LIGO/Virgo band. Only those from very massive NC with high velocity dispersion are likely to remain eccentric up to the high frequency band. Note that we have computed the orbital evolution only up to the pericentre distance of  $4 R_{\text{Sch}}$  and some extreme binaries will not emit GW signal higher than 30 Hz. This could be an artifact of using post-Newtonian approximation. Eventually the binaries in this regime should emit gravitational waves at higher frequencies than 30 Hz. We simply refer to East et al. (2013) for the derivation of more realistic derivation of the waveforms for eccentric binaries and their detectability with the ground-based GW detectors.

## 8 SUMMARY AND CONCLUSION

We have generated  $N$ -body realizations for nuclear star clusters (NCs) located at the centre of galactic bulges and hosting a massive black hole (MBH). In our simulations, the surrounding bulge is considered as the external potential well which makes the velocity dispersion of the embedded star cluster isothermal since a deep potential well behaves like a heat bath (Yoon et al. 2011). The MBH, in the same manner, is also modeled as a point-mass potential but growing with time to ensure the adiabatic adjustment of the stellar system. Consequently, our  $N$ -body realizations have a stellar density cusp ( $\rho \sim r^{-1.75}$ ; Bahcall & Wolf 1976) and Keplerian velocity dispersion within the radius of influence. In addition, the overall velocity structure is similar to observations of the star cluster at the centre of Milky Way (e.g., Schödel et al. 2009). Strictly speaking, however, these star clusters are not in equilibrium but expand continuously since the MBH can generate kinetic energies by the interaction with stars in the cusp. The slopes of density and velocity dispersion profiles of our  $N$ -body realizations are slightly shallower than those of theoretical expectations.

This environment of NCs is a good laboratory for gravitational wave (GW) sources. In order to investigate GW event rates in NCs, we have collected the orbital information of close encounters (i.e., semi-major axis and eccentricity) in our  $N$ -body simulations. While most of binaries are disrupted by the strong tidal field from MBH, there can be many hyperbolic encounters of stellar mass black holes (BHs) whose pericentre distances are sufficiently small to radiate GWs efficiently due to the high density and velocity dispersion at the vicinity of the MBH and the high number fraction of BHs due to the mass segregation (Hopman & Alexander 2006; O’Leary et al. 2009). When the energy loss by gravitational radiation (GR) is greater than the orbital energy, two BHs make a binary and merge quickly because of the small separation and large eccentricity after capture. Thus, the capture event rate corresponds to the merger rate. The capture happens most frequently near the half mass radius rather than within the radius of influence. Thus, our investigation of GR capture event rates is still valid although

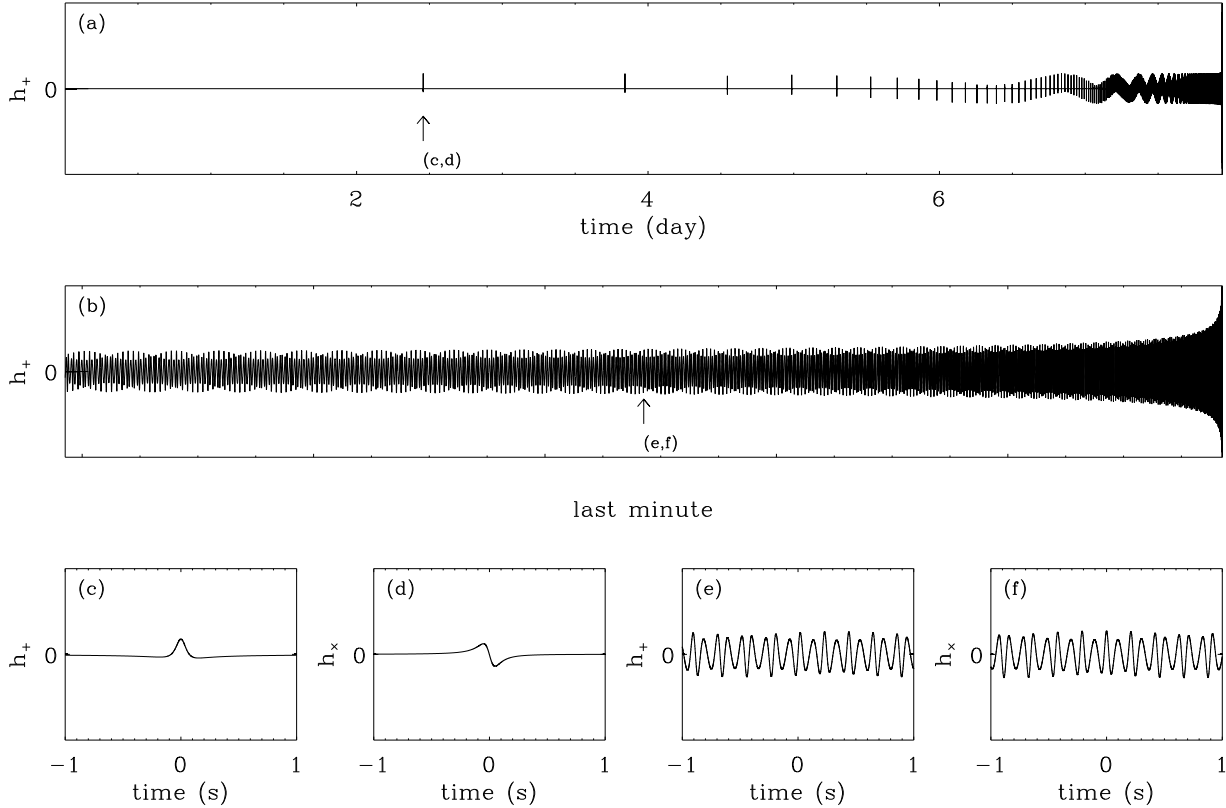


**Figure 18.** Waveform of BH-BH binary coalescence for the same binary in Fig 17. (a)  $h_+$  for whole stage. The merging time is  $\sim 8$  days. The waveform is like a burst, initially. (b)  $h_+$  for last minute. The waveform is much sinusoidal at this time. (c,d)  $h_+$  and  $h_x$  for the first burst as marked in (a). They are similar to those of eccentric binaries in Abramovici et al. (1992). (e,f)  $h_+$  and  $h_x$  at a half minute before coalescence as marked in (b). At this time, the frequency is  $\sim 10$  Hz.

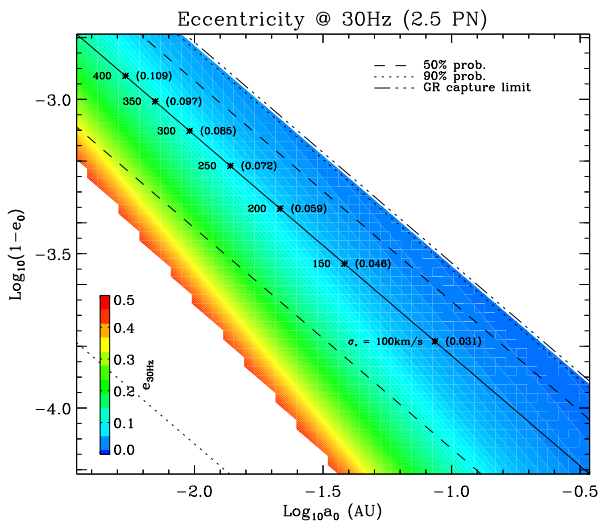


**Figure 19.** Eccentricity of BH binaries at 30 Hz which is the typical low frequency limit of ground based detectors, in the initial  $(a_0, e_0)$  plane. The eccentricity at 30 Hz is expressed by the color and the diagonal solid line represents the typical values of  $(a_0, e_0)$  for different  $\sigma_*$ . We limited the range of calculation down to 10% of the probability peak of the initial probability distribution function of the initial eccentricity for a given velocity dispersion marked at the central solid line. Also we show the locus of 50 % of the peak as broken lines.

our models can not precisely realize the cluster inside of the radius of influence. By counting the number of GR capture events, we have built scaling relations of merger rates for a NC as a function of the mass of the MBH and the velocity dispersion of the star cluster. As the result, the merger rate for a Milky-Way-like galaxy is  $\sim 10^{-10} \text{ yr}^{-1}$  proportional to the mass ratio of MBH to the star cluster.

From the  $M_{\text{MBH}} - \sigma_*$  relation (e.g., Tremaine et al. 2002), the merger rate becomes a function of the mass of MBH only. By using realistic mass function of MBHs (e.g., Aller & Richstone 2002), we have determined the merger rate density per unit volume. Then, the detection rates can be expressed with the merger rate density and the size of cosmological volume covered by GW detectors if we simply assume the uniformness of merger events over cosmic time and volume. We have obtained the expected detection rates  $0.02 \sim 14 \text{ yr}^{-1}$  for advanced LIGO depending on the maximum horizon distances from different studies (Baker et al. 2007; Reisswig et al. 2009; Abadie et al. 2010) and the mass ratio of MBH to the star cluster 0.1 and 0.2. This estimate can cover those of O’Leary et al. (2009) who suggested the detection rate of  $\sim 5 - 20 \text{ yr}^{-1}$  of 5 to 15  $M_{\odot}$  BH-BH binary coalescences in galactic nuclei for advanced LIGO. However, this study still have some limitations; (1) It is necessary to consider realistic mass function for BHs instead of assuming the mean mass fraction of BHs. (2) There is a relation between the mass of MBHs and the NCs (Graham & Spitler 2009). However, we fixed the mass ratio

of MBH to the star cluster to 0.1 and 0.2. (3) In order to determine the maximum horizon distance for BH-BH binary mergers, the precise signal-to-noise ratio calculation is needed.

We have investigated the statistics of coalescing BH-BH binaries and found that the typical semi-major axis and eccentricity of these binaries are related to the velocity dispersion of the system. We also have implemented the post-Newtonian (PN) approximation on the two body motions up to 2.5PN orders. With a given set of semi-major axis and eccentricity, we calculated the two-body motion under the PN approximation and the waveform of GW emission. The merging time is about a few hours for a typical BH-BH binaries in a Milky-Way-like galaxy. We also estimated the eccentricities of GR captured binaries when they enter the LIGO/Virgo band (assumed to be 30Hz). Most of the binaries formed in relatively low velocity environment ( $\sigma_* \sim 100$  km/s) would become nearly circular while those formed in very high velocity environment are likely to keep significant eccentricity when they cross the 30 Hz. Considering the fact that the low velocity galaxies contribute more to the total merger rate (cf. equation 35), the GR captured binaries are likely to be indistinguishable from those of different origin in the sense the eccentricity effect is nearly negligible.

## ACKNOWLEDGMENTS

This work was supported by the National Research Foundation of Korea (NRF) grant NRF-2006-0093852 funded by the Korean government. HML acknowledges Alexander von Humboldt Foundation for the Research Award in 2013.

## APPENDIX A. POST NEWTONIAN EQUATION OF MOTION IN CENTER OF MASS FRAME

Here, we present the post Newtonian (PN) equation of motion of binary system in the centre of mass frame up to 2.5PN order by following Mora & Will (2004) (also see Appendix in Brem et al. 2014). Because we assume non-spinning BHs, we do not consider spin terms in this paper. For the beginning, we borrow notations from Mora & Will (2004) as

$$\begin{aligned} m &= m_1 + m_2, \\ \mathbf{v} &= \mathbf{v}_2 - \mathbf{v}_1, \\ \mathbf{r} &= \mathbf{r}_2 - \mathbf{r}_1, \\ \mathbf{n} &= \mathbf{r}/r, \\ \eta &= (m_1 m_2)/(m_1 + m_2)^2 \end{aligned} \quad (46)$$

where  $m_1$  and  $m_2$  are the mass of stars,  $\mathbf{r}_1$ ,  $\mathbf{r}_2$ ,  $\mathbf{v}_1$  and  $\mathbf{v}_2$  are the 3-dimensional positions and velocities, and  $\eta$  is the symmetric mass ratio. As mentioned in the text, the PN acceleration can be considered as a perturbation and added to the gravitational acceleration as

$$\mathbf{a} = \mathbf{a}_n + \mathbf{a}_{\text{pn}} = -\frac{m}{r^2} \mathbf{n} + \frac{m}{r^2} (A \mathbf{n} + B \mathbf{v}) \quad (47)$$

where  $A$  and  $B$  are the PN coefficients related to the relative position and velocity, respectively, where

$$A_1 = 2(2 + \eta) \frac{m}{r} - (1 + 3\eta)v^2 + \frac{3}{2}\eta \dot{r}^2, \quad (48)$$

$$\begin{aligned} A_2 &= -\frac{3}{4}(12 + 29\eta) \frac{m^2}{r^2} - \eta(3 - 4\eta)v^4 - \frac{15}{8}\eta(1 - 3\eta)\dot{r}^4 \\ &\quad + \frac{1}{2}\eta(13 - 4\eta) \frac{m}{r} v^2 + (2 + 25\eta + 2\eta^2) \frac{m}{r} \dot{r}^2 \\ &\quad + \frac{3}{2}\eta(3 - 4\eta)v^2 \dot{r}^2, \end{aligned} \quad (49)$$

$$A_{5/2} = \frac{8}{5}\eta \frac{m}{r} \dot{r} \left( \frac{17}{3} \frac{m}{r} + 3v^2 \right) \quad (50)$$

and

$$B_1 = 2(2 - \eta)\dot{r}, \quad (51)$$

$$B_2 = -\frac{1}{2}(4 + 41\eta + 8\eta^2) \frac{m}{r} \dot{r} + \frac{1}{2}\eta(15 + 4\eta)v^2 \dot{r} - \frac{3}{2}\eta(3 + 2\eta)\dot{r}^3, \quad (52)$$

$$B_{5/2} = -\frac{8}{5}\eta \frac{m}{r} \left( 3 \frac{m}{r} + v^2 \right) \quad (53)$$

where  $\dot{r}$  is the first time derivative of radial distance defined as  $\dot{r} = \mathbf{r} \cdot \mathbf{v}/r$ . Then the coefficients  $A$  and  $B$  are given by the summations of coefficients for different PN order divided by the speed of light  $c$ ,  $A_i/c^{2i}$ . Note that the sign of  $B$  is opposite of that in Blanchet & Iyer (2003).

Since the NBODY code uses 4th-order Hermite integrator, we have to have the first time derivatives of accelerations as similar to the accelerations

$$\dot{\mathbf{a}} = \dot{\mathbf{a}}_n + \dot{\mathbf{a}}_{\text{pn}}. \quad (54)$$

The derivative of PN acceleration  $\dot{\mathbf{a}}_{\text{pn}}$  can be expressed as

$$\dot{\mathbf{a}}_{\text{pn}} = -2 \frac{m}{r^3} \dot{r} (A \mathbf{n} + B \mathbf{v}) + \frac{m}{r^2} (\dot{A} \mathbf{n} + \dot{B} \mathbf{v} + A(\mathbf{v}/r - \mathbf{n}\dot{r}/r) + B \mathbf{a}) \quad (55)$$

where  $\dot{A}$  and  $\dot{B}$  are the time derivatives of the coefficients  $A$  and  $B$ , which are the summations of

$$\dot{A}_1 = -2(2 + \eta) \frac{m}{r^2} \dot{r} - 2(1 + 3\eta) \mathbf{v} \cdot \mathbf{a} + 3\eta \dot{r} \ddot{r}, \quad (56)$$

$$\begin{aligned} \dot{A}_2 &= \frac{3}{2}(12 + 29\eta) \frac{m^2}{r^3} \dot{r} - 4\eta(3 - 4\eta)v^2 \mathbf{v} \cdot \mathbf{a} \\ &\quad - \frac{15}{2}\eta(1 - 3\eta)\dot{r}^3 \ddot{r} + \frac{1}{2}\eta(13 - 4\eta) \frac{m}{r} \left( 2\mathbf{v} \cdot \mathbf{a} - \frac{v^2 \dot{r}}{r} \right) \\ &\quad + (2 + 25\eta + 2\eta^2) \frac{m}{r} \left( 2\dot{r} \ddot{r} - \frac{\dot{r}^3}{r} \right) \\ &\quad + 3\eta(3 - 4\eta)(\mathbf{v} \cdot \mathbf{a} \dot{r}^2 + v^2 \dot{r} \ddot{r}), \end{aligned} \quad (57)$$

$$\begin{aligned} \dot{A}_{5/2} &= \frac{8}{5}\eta \frac{m}{r} \left( \ddot{r} - \frac{\dot{r}^2}{r} \right) \left( \frac{17}{3} \frac{m}{r} + 3v^2 \right) \\ &\quad + \frac{8}{5}\eta \frac{m}{r} \dot{r} \left( -\frac{17}{3} \frac{m}{r^2} \dot{r} + 6\mathbf{v} \cdot \mathbf{a} \right) \end{aligned} \quad (58)$$

and

$$\dot{B}_1 = 2(2 - \eta)\ddot{r}, \quad (59)$$

$$\begin{aligned} \dot{B}_2 &= -\frac{1}{2}(4 + 41\eta + 8\eta^2) \frac{m}{r} \left( \ddot{r} - \frac{\dot{r}^2}{r} \right) \\ &\quad + \frac{1}{2}\eta(15 + 4\eta)(2\mathbf{v} \cdot \mathbf{a} \dot{r} + v^2 \ddot{r}) - \frac{9}{2}\eta(3 + 2\eta)\dot{r}^2 \ddot{r}, \end{aligned} \quad (60)$$



$$\dot{B}_{5/2} = \frac{8}{5}\eta\frac{m}{r^2}\dot{r}\left(3\frac{m}{r} + v^2\right) - \frac{8}{5}\eta\frac{m}{r}\left(-3\frac{m}{r^2}\dot{r} + 2\mathbf{v} \cdot \mathbf{a}\right) \quad (61)$$

where  $\ddot{r}$  is the second time derivative of the radial distance given by

$$\ddot{r} = (v^2 + \mathbf{r} \cdot \mathbf{a} - \dot{r}^2)/r. \quad (62)$$

## REFERENCES

- Aarseth, S. J. 1999, *PASP*, 111, 1333
- Aarseth, S. J. 2007, *MNRAS*, 378, 285
- Aarseth, S. J. 2010, *Gravitational N-Body Simulations*, by Sverre J. Aarseth, Cambridge, UK: Cambridge University Press, 2010,
- Abadie, J., Abbott, B. P., Abbott, R., et al. 2010, *Classical and Quantum Gravity*, 27, 173001
- Abramovici, A., Althouse, W. E., Drever, R. W. P., et al. 1992, *Science*, 256, 325
- Alexander, T. 2005, *Phys. Rep.*, 419, 65
- Aller, M. C., & Richstone, D. 2002, *AJ*, 124, 3035
- Ananda, K. N., Clarkson, C., & Wands, D. 2007, *Phys. Rev. D*, 75, 123518
- Andersson, N., Ferrari, V., Jones, D. I., et al. 2011, *General Relativity and Gravitation*, 43, 409
- Antonini, F., & Perets, H. B. 2012, *ApJ*, 757, 27
- Bae, Y., Lee, H. M., Kim, C. 2014, *MNRAS*, 440, 2714
- Bahcall, J. N., & Wolf, R. A. 1976, *ApJ*, 209, 214
- Baker, J. G., McWilliams, S. T., van Meter, J. R., et al. 2007, *Phys. Rev. D*, 75, 124024
- Balcells, M., Graham, A. W., Domínguez-Palmero, L., & Peletier, R. F. 2003, *ApJ*, 582, L79
- Barth, A. J., Greene, J. E., & Ho, L. C. 2005, *ApJ*, 619, L151
- Banerjee, S., Baumgardt, H., & Kroupa, P. 2010, *MNRAS*, 402, 371
- Baumgardt, H., Makino, J., & Ebisuzaki, T. 2004a, *ApJ*, 613, 1133
- Baumgardt, H., Makino, J., & Ebisuzaki, T. 2004b, *ApJ*, 613, 1143
- Belczynski, K., Taam, R. E., Kalogera, V., Rasio, F. A., & Bulik, T. 2007, *ApJ*, 662, 504
- Berentzen, I., Preto, M., Berczik, P., Merritt, D., & Spurzem, R. 2009, *ApJ*, 695, 455
- Binney, J., & Tremaine, S. 2008, *Galactic Dynamics: Second Edition*, Princeton University Press, Princeton, NJ
- Blanchet, L., & Iyer, B. R. 2003, *Classical and Quantum Gravity*, 20, 755
- Böker, T., Laine, S., van der Marel, R. P., et al. 2002, *AJ*, 123, 1389
- Böker, T., Sarzi, M., McLaughlin, D. E., et al. 2004, *AJ*, 127, 105
- Brem, P., Amaro-Seoane, P., & Sopena, C. F. 2014, *MNRAS*, 437, 1259
- Carollo, C. M., Stiavelli, M., de Zeeuw, P. T., & Mack, J. 1997, *AJ*, 114, 2366
- Côté, P., Blakeslee, J. P., Ferrarese, L., et al. 2004, *ApJS*, 153, 223
- Côté, P., Piatek, S., Ferrarese, L., et al. 2006, *ApJS*, 165, 57
- Dehnen, W. 1993, *MNRAS*, 265, 250
- Downing, J. M. B., Benacquista, M. J., Giersz, M., & Spurzem, R. 2011, *MNRAS*, 416, 133
- East, W. E., McWilliams, S. T., Levin, J., & Pretorius, F., 2013, *Phys. Rev. D*, 87, 043004
- Einstein, A. 1916, *Sitzungsberichte der Königlich Preußischen Akademie der Wissenschaften (Berlin)*, 688
- Ferrarese, L., & Ford, H. 2005, *Space Sci. Rev.*, 116, 523
- Fiestas, J., Porth, O., Berczik, P., & Spurzem, R. 2012, *MNRAS*, 419, 57
- Freitag, M., Amaro-Seoane, P., & Kalogera, V. 2006, *ApJ*, 649, 91
- Giersz, M., & Hoggie, D. C. 1996, *MNRAS*, 279, 1037
- Goodman, J., & Binney, J. 1984, *MNRAS*, 207, 511
- Graham, A. W., & Driver, S. P. 2007, *MNRAS*, 380, L15
- Graham, A. W., & Scott, N. 2015, *ApJ*, 798, 54
- Graham, A. W., & Spitler, L. R. 2009, *MNRAS*, 397, 2148
- Hansen, R. O. 1972, *Phys. Rev. D*, 5, 1021
- Holley-Bockelmann, K., Mihos, J. C., Sigurdsson, S., Hernquist, L., & Norman, C. 2002, *ApJ*, 567, 817
- Hopman, C., & Alexander, T. 2006, *ApJ*, 645, L133
- Hulse, R. A., & Taylor, J. H. 1974, *ApJ*, 191, L59
- Kalogera, V., Kim, C., Lorimer, D. R., et al. 2004, *ApJ*, 601, L179
- Kang, W.-R., Woo, J.-H., Schulze, A., et al. 2013, *ApJ*, 767, 26
- Kent, S. M. 1992, *ApJ*, 387, 181
- Kidder, L. E. 1995, *Phys. Rev. D*, 52, 821
- Kormendy, J., & Richstone, D. 1995, *ARA&A*, 33, 581
- Kozai, Y. 1962, *AJ*, 67, 591
- Lee, H. M., & Ostriker, J. P. 1986, *ApJ*, 310, 176
- Lee, M. H. 1993, *ApJ*, 418, 147
- Lin, D. N. C., & Tremaine, S. 1980, *ApJ*, 242, 789
- Lincoln, C. W., & Will, C. M. 1990, *Phys. Rev. D*, 42, 1123
- McConnell, N. J., & Ma, C.-P. 2013, *ApJ*, 764, 184
- Merritt, D., Alexander, T., Mikkola, S., & Will, C. M. 2011, *Phys. Rev. D*, 84, 044024
- Merritt, D., Mikkola, S., & Szell, A. 2007, *ApJ*, 671, 53
- Mora, T., & Will, C. M. 2004, *Phys. Rev. D*, 69, 104021
- Mueller, E., & Janka, H.-T. 1997, *A&A*, 317, 140
- Nitadori, K., & Aarseth, S. J. 2012, *MNRAS*, 424, 545
- O’Leary, R. M., Kocsis, B., & Loeb, A. 2009, *MNRAS*, 395, 2127
- O’Leary, R. M., Rasio, F. A., Fregeau, J. M., Ivanova, N., & O’Shaughnessy, R. 2006, *ApJ*, 637, 937
- O’Shaughnessy, R., & Kim, C., 2010, *ApJ*, 715, 230
- Peters, P. C. 1964, *Physical Review*, 136, 1224
- Peters, P. C., & Mathews, J. 1963, *Physical Review*, 131, 435
- Quinlan, G. D., & Shapiro, S. L. 1987, *ApJ*, 321, 199
- Quinlan, G. D., & Shapiro, S. L. 1989, *ApJ*, 343, 725
- Quinlan, G. D., Hernquist, L., & Sigurdsson, S. 1995, *ApJ*, 440, 554
- Reisswig, C., Husa, S., Rezzolla, L., et al. 2009, *Phys. Rev. D*, 80, 124026
- Schödel, R., Merritt, D., & Eckart, A. 2009, *A&A*, 502, 91
- Shapiro, S. L. 1977, *ApJ*, 217, 281
- Sigurdsson, S., Hernquist, L., & Quinlan, G. D. 1995, *ApJ*, 446, 75
- Spitzer, L. 1987, Princeton, NJ, Princeton University Press, 1987, 191 p.,
- Takahashi, K., Lee, H. M., & Inagaki, S. 1997, *MNRAS*, 292, 331
- Tremaine, S., Gebhardt, K., Bender, R., et al. 2002, *ApJ*, 574, 740
- Tsang, D., 2013, *ApJ*, 777, 203
- Walcher, C. J., van der Marel, R. P., McLaughlin, D., et al. 2005, *ApJ*, 618, 237
- Weisberg, J. M., & Taylor, J. H. 2005, *Binary Radio Pulsars*, 328, 25
- Yakunin, K. N., Marronetti, P., Mezzacappa, A., et al. 2010, *Classical and Quantum Gravity*, 27, 194005
- Yoon, I., Lee, H. M., & Hong, J. 2011, *MNRAS*, 414, 2728
- Young, P. 1980, *ApJ*, 242, 1232